

Abstract

Apart from single gravitational wave (GW) events, those with a smaller amplitude produce a stochastic GW background. This has not been measured yet using traditional GW detectors, like the Laser Interferometer Gravitational-Wave Observatory (LIGO), Virgo or the Kamioka Gravitational Wave Detector (KAGRA). With future detectors, such as Einstein Telescope (ET) or Cosmic Explorer (CE), it is expected to be observed in the frequency range of $\approx 10 - 10^4$ Hz. The astrophysical gravitational wave background (AGWB) is modelled here in a frequency-dependent way using the `Multi_CLASS` code. We assume the design noise of a cross-correlation between ET and CE at the dipole and use this as the variance of a Gaussian noise profile. Then, we use Information Field Theory (IFT) to separate our calculated power spectra from this noise. This returns some possible reconstruction at a high AGWB power spectrum at 400 Hertz but does not work for a lower power spectrum at 100 Hertz. We also use this method with the cosmological background anisotropies from `CLASS_GWB`, where the noise is comparatively too high for a successful reconstruction.

List of Abbreviations

AGWB	Astrophysical Gravitational Wave Background
BBH	Binary Black Hole
BH	Black Hole
CE	Cosmic Explorer
CGWB	Cosmological Gravitational Wave Background
CLASS	Cosmic Linear Anisotropy Solving System
ET	Einstein Telescope
GW	Gravitational Wave
GWTC	Gravitational Wave Transient Catalogue
HMF	Halo Mass Function
IFT	Information Field Theory
KAGRA	Kamioka Gravitational Wave Detector
LIGO	Laser Interferometer Gravitational-Wave Observatory
NANOGrav	North American Nanohertz Observatory for Gravitational Waves
NIFTy	Numerical Information Field TheorY
SFR	Star Formation Rate

Contents

List of Abbreviations	2
1 Introduction	5
2 Gravitational Waves	7
2.1 Fundamentals	7
2.1.1 Wave Equation	7
2.1.2 Free Field Modes	8
2.1.3 Quadrupole Wave Emission	9
2.2 Stochastic Background	11
2.2.1 Astrophysical	11
Binary Black Hole Mergers	12
Dipole	13
2.2.2 Cosmological	14
Inflation	15
2.2.3 Number Density Distribution	15
2.2.4 Projection Effects	16
3 Frequency Dependence of the AGWB	19
3.1 Energy Spectrum	19
3.2 Star Formation Rate	23
3.3 Halo Mass Function	25
3.4 Merger Rate	27
3.5 Window Function	28
3.6 Bias & Magnification Bias	32
3.7 Evolution Bias	32
4 Instrumental Noise	34
4.1 LIGO, Virgo & KAGRA	34
4.2 Einstein Telescope & Cosmic Explorer	35
5 Information Field Theory	37
5.1 Information Hamiltonian	38
5.2 Wiener Filter	38
5.3 1D Toy Model	39
6 Results	40

6.1	Frequency Dependent AGWB Angular Power Spectrum	40
6.2	AGWB vs. Noise	42
6.3	CGWB vs. Noise	47
7	Conclusion & Outlook	51
A	Call Graph? (TODO)	52
	List of Figures	54
	List of Tables	55
	Acknowledgements	56
	Bibliography	57

1

Introduction

Most large-scale structure surveys, like Planck [planck_collaboration_planck_2016](#), have found an unexpectedly large dipole anisotropy, which can be used to test the cosmological principle. The principle states that the universe is isotropic and homogeneous on large scales. These surveys have error sources, such as partial sky covering due to masking sources and the fact that clustering of matter can produce a dipole contribution.

Gravitational waves have a very high sky coverage since masking is not necessary for GW detectors. Thus, we can use GW observations to test the cosmological principle in an independent way. To do this, we can look at the astrophysical gravitational wave background (AGWB), specifically compact binary mergers. They are expected to make up the majority of the GW background. This background has been detected in a low-frequency range of $10^{-8.75} - 10^{-7.5}$ Hz.

Many GW have an amplitude below the necessary signal-to-noise ratio to be detected individually. These sources form the GW background. The first detection of this background was made in 2023 by the NANOGrav pulsar time array with an energy density parameter of $\Omega_{GW} = 9.3_{-4.0}^{+5.8} \cdot 10^{-9}$ [Agazie et al. 2023](#). In current GW experiments, like LIGO, Virgo and KAGRA, the noise is too high to detect this background. Experiments with a higher sensitivity are planned for the future, like the ground-based Einstein Telescope (ET) and Cosmic Explorer (CE). These might have low enough noise to detect the GW background and even disentangle different components.

With new detectors in the future we could measure intrinsic anisotropies in this background which are not coming from our observer motion or statistical properties, so-called shot noise from a Poisson distribution. These anisotropies, like for example the dipole, would contradict the cosmological principle. It states that the universe is homogeneous and isotropic at every point.

We compute the anisotropies of the (AGWB) in a frequency-dependent way using a modified version of [CLASS](#) Blas, Lesgourgues, and Tram 2011, an Einstein-Boltzmann solver. It makes sense to use an Einstein-Boltzmann solver since the formalism of computing the angular power spectrum is similar to doing this for galaxy counts. Then, we use a separation method from information field theory (IFT) on the AGWB at different frequencies, as well as on the cosmological GW background.

We find that the signal can be partly recovered for the AGWB at frequencies with a high angular power spectrum. However, for most frequencies of the AGWB,

as well as for the cosmological background, the separation does not work.

This thesis is structured as follows: In Chapter 2, we discuss the fundamental physics of GW and their stochastic background. Then, the frequency dependence of the AGWB is explained in Chapter 3. The instrumental noise of current and future experiments is presented in Chapter 4. IFT and the used techniques are summarised in Chapter 5. Then, we present the results in Chapter 6 before concluding and giving an outlook.

2

Gravitational Waves

2.1 Fundamentals

GW are oscillations in spacetime, similar to electromagnetic waves. We can start with the Einstein equation:

$$G_{\mu\nu} = \frac{8\pi G}{c^4} T_{\mu\nu}. \quad (2.1)$$

Since GW (mostly) propagate in the vacuum and we assume a small amplitude $|\delta g_{\mu\nu}| \ll 1$, we arrive at the following differential equation.

$$T_{\mu\nu} = 0 \quad (2.2)$$

$$\Rightarrow G_{\mu\nu} = 0 \quad (2.3)$$

We assume that the metric only has small linear perturbations.

$$g_{\mu\nu}(t, \vec{x}) = \bar{g}_{\mu\nu}(t) + \delta g_{\mu\nu}(t, \vec{x}) \quad (2.4)$$

$$= \eta_{\mu\nu} + 2\kappa h_{\mu\nu} \quad (2.5)$$

$$\kappa = \frac{\sqrt{8\pi G}}{c^2} \approx 2.1 \cdot 10^{-41} \frac{\text{s}^2}{\text{kg m}} \quad (2.6)$$

$$|h_{\mu\nu}| \ll 1 \quad (2.7)$$

Here $\eta_{\mu\nu}$ the Minkowski metric for flat spacetime.

We can solve the differential equation with the trace reverse tensor.

$$\bar{h}_{\mu\nu} = h_{\mu\nu} - \frac{1}{2}\eta_{\mu\nu}h \quad (2.8)$$

Here, h is the trace of $h_{\mu\nu}$.

2.1.1 Wave Equation

If we want to describe the transport of energy and momentum by GW analytically, we can assume an asymptotically flat environment since the detector is at a far distance from the source. Then, we will consider Newtonian binaries in a circular orbit and

only look at the non-relativistic regime. This will limit us to the inspiral phase, see Fig. 2.3 since the non-relativistic approximation only applies in that phase. Later though, we will see that for the implementation in the CLASS code all the phases need to be modelled.

The linear perturbation $h_{\mu\nu}$ is a dimensionless bosonic tensor field and thus follows the massless field equation (Holten 2019):

$$\square h_{\mu\nu} - \partial_m u \partial^\lambda h_{\lambda\nu} - \partial_\nu \partial^\lambda h_{\lambda\mu} + \partial_\mu \partial_\nu h - \eta_{\mu\nu} (\square h - \partial^\kappa \partial^\lambda h_{\kappa\lambda}) = -\kappa T_{\mu\nu} \quad (2.9)$$

For the gauge transformation, we can impose the de Donder gauge condition:

$$\partial^\mu h_{\mu\nu} = \frac{1}{2} \partial_\nu h^\mu. \quad (2.10)$$

This simplifies the wave equation to the following form with the trace reverse tensor (2.8).

$$\partial^\mu \underline{h}_{\mu\nu} = 0 \quad (2.11)$$

$$\Rightarrow \square \underline{h}_{\mu\nu} = -\kappa T_{\mu\nu} \quad (2.12)$$

We can also choose h to be traceless, which leads to h and \underline{h} coinciding.

$$h = h^\mu_\mu := 0 \quad (2.13)$$

$$\Rightarrow \underline{h}_{\mu\nu} = h_{\mu\nu} \quad (2.14)$$

$$\Rightarrow \underline{h} = \underline{h}^\mu_\mu = 0 \quad (2.15)$$

2.1.2 Free Field Modes

Now, we can perform a Fourier decomposition of the linear perturbation.

$$\underline{h}_{\mu\nu}(x) = \int \frac{d^4 k}{(2\pi)^2} \epsilon_{\mu\nu}(k) e^{-ikx} \quad (2.16)$$

$$k = (\omega, \vec{k}) \quad (2.17)$$

The field equation is invariant under the following gauge transformation.

$$\epsilon'_{\mu\nu} = \epsilon_{\mu\nu} + k_\mu \alpha_\nu + k_\nu \alpha_\mu - \eta_{\mu\nu} k^\lambda \alpha_\lambda \quad (2.18)$$

Since k is the wave vector and GW propagate with the speed of light, it has to be a light-like four-vector.

$$k^2 = 0 \quad (2.19)$$

$$\Rightarrow \epsilon_{\mu\nu}(k) = e_{\mu\nu}(k) \delta(k^2) \quad (2.20)$$

To get a simplified amplitude form, we choose α from the gauge condition 2.18 in such a way that we eliminate e'_{00} , e'_{i0} and e'_{ii} .

$$\epsilon'_{\mu\nu}(k) = e'_{\mu\nu}(k)\delta(k^2) \quad (2.21)$$

For a wave propagating in z-direction, we will then get the following amplitude form.

$$e'_{\mu\nu}(\omega, \vec{k}) = \begin{pmatrix} 0 & 0 & 0 & 0 \\ 0 & e_+(\omega) & e_x(\omega) & 0 \\ 0 & e_x(\omega) & -e_+(\omega) & 0 \\ 0 & 0 & 0 & 0 \end{pmatrix} \quad (2.22)$$

To illustrate plus and cross polarisations, Fig. 2.1 shows both over one period.

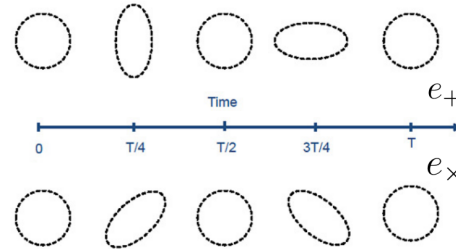


Figure 2.1: Illustration of the plus and cross polarisations varying with time. The figure is taken from a lecture by Prof. Jan van Holten.

Then, a plane wave in z-direction with plus polarisation would have the following expression, since the cross polarisation will be zero.

$$h(z, t) = h_+ \begin{pmatrix} 0 & 0 & 0 & 0 \\ 0 & 1 & 0 & 0 \\ 0 & 0 & -1 & 0 \\ 0 & 0 & 0 & 0 \end{pmatrix} e^{i(kz - \omega t)} \quad (2.23)$$

For a length of L_0 along the x-axis, it would oscillate in size in the following way:

$$L(t) = L_0 + \frac{h_+ L_0}{2} \cos(\omega t). \quad (2.24)$$

2.1.3 Quadrupole Wave Emission

If we have a source in a finite region of space, we can use the retarded Green's function to solve the wave equation. This is because the waves are causally related to the source $t > |\vec{x}' - \vec{x}|$.

$$\square \underline{h}_{\mu\nu} = -\kappa T_{\mu\nu} \quad (2.25)$$

$$\Rightarrow \underline{h}_{\mu\nu}(\vec{x}, t) = \frac{\kappa}{4\pi} \int d^3x' \frac{T_{\mu\nu}(\vec{x}', t - |\vec{x}' - \vec{x}|)}{|\vec{x}' - \vec{x}|} \quad (2.26)$$

Then, we can assume that we are in the far field regime, such that $|\vec{x}| \gg |\vec{x}'|$.

$$r := |\vec{x}| \approx |\vec{x}' - \vec{x}| \quad (2.27)$$

$$\Rightarrow \underline{h}_{\mu\nu}(\vec{x}, t) = \frac{\kappa}{4\pi r} \int d^3x' T_{\mu\nu}(\vec{x}', t - r) \quad (2.28)$$

If we consider a localised source, the solution does not have a dynamical time component, i.e. $\partial_0 h_{0j} = 0$ (Holten 2019). Additionally to the de Donder gauge (2.10), we will now impose the traceless-transverse (TT) gauge, which implies transversality.

$$r_i \underline{h}_{ij} = 0 \quad (2.29)$$

$$h_{ii} = 0 \quad (2.30)$$

This gives us the following solution which is valid at a large distance in empty space.

$$\underline{h}_{ij}(\vec{x}, t) = \frac{\kappa}{4\pi} (\delta_{ik} - \hat{r}_i \hat{r}_k)(\delta_{jl} - \hat{r}_j \hat{r}_l) \left(I_{kl} + \frac{1}{2} \delta_{kl} \vec{r} \underline{I} \vec{r} \right) \quad (2.31)$$

I_{ij} is the quadrupole moment of the total energy density:

$$I_{ij}(t - r) = \int d^3x' \left(T_{ij} - \frac{1}{3} \delta_{ij} T_{kk} \right) T_{00}(\vec{x}', t - r). \quad (2.32)$$

$$= \frac{1}{2} \partial_0^2 \int d^3x' \left(x'_i x'_j - \frac{1}{3} \delta_{ij} \vec{x}'^2 \right) T_{00}(\vec{x}', t - r). \quad (2.33)$$

The last equation follows since the time derivative is equal to the derivative with respect to the retarded time $u = t - r$.

$$\partial_0 = \partial_u \quad (2.34)$$

$$\Rightarrow \partial_0^2 T_{00}(\vec{x}', u) = \partial_0 \partial'_i T_{i0}(\vec{x}', u) = \partial'_i \partial'_j T_{ij}(\vec{x}', u) \quad (2.35)$$

As mentioned earlier, we can perform a non-relativistic approximation for the inspiral phase. In this case, the energy density is dominated by the mass density. We can thus rewrite \underline{h}_{ij} with the mass quadrupole moment.

$$I_{ij} = \frac{1}{2} \frac{\partial^2 Q_{ij}}{\partial t^2} \quad (2.36)$$

$$Q_{ij}(t - r) = \frac{1}{2} \int d^3x' \left(x'_i x'_j - \frac{1}{3} \delta_{ij} \vec{x}'^2 \right) \rho(\vec{x}', t - r) \quad (2.37)$$

GW cannot form from a dipole mass distribution since that would require negative masses. However, if we have a quadrupole distribution with vacuum and masses (like a binary black hole for example), GW can be created.

The wave field for non-relativistic sources is thus:

$$\underline{h}_{ij}(\vec{x}, t) = \frac{\kappa}{8\pi} (\delta_{ik} - \hat{r}_i \hat{r}_k)(\delta_{jl} - \hat{r}_j \hat{r}_l) \frac{\partial^2}{\partial t^2} \left(Q_{kl} + \frac{1}{2} \delta_{kl} \vec{r} \underline{Q} \vec{r} \right) \quad (2.38)$$

2.2 Stochastic Background

The stochastic GW background consists of all sources that are too faint to be resolved individually, thus it is a superposition of many independent sources. The same source can contribute to multiple frequencies over time. The biggest background comes from astrophysical sources, like compact object mergers, but there is also a smaller cosmological background present. That one originates from early universe phenomena. To measure the background we need the correlation between two detector outputs Christensen 2019. If the noise between them is uncorrelated, it will average out over time and leave the background signal.

$$\langle s_1(t)s_2(t) \rangle = \langle (n_1(t) + h(t))(n_2(t) + h(t)) \rangle \quad (2.39)$$

$$= \langle n_1(t)n_2(t) \rangle + \langle n_1(t)h(t) \rangle + \langle h(t)n_2(t) \rangle + \langle h(t)h(t) \rangle \quad (2.40)$$

$$\approx \langle h(t)h(t) \rangle \quad (2.41)$$

From there we can compute the root mean square of the strain.

$$h_{rms}^2 = \left\langle \sum_{i,j} h_{ij}h_{ij} \right\rangle \quad (2.42)$$

$$= \int_0^\infty df S_h(f) \quad (2.43)$$

Here S_h is the spectral density, from which we can derive the GW energy density.

$$\rho_{GW} = \int_0^\infty df S_h(f) \frac{\pi c^2 f^2}{8G} \quad (2.44)$$

The frequency-dependent monopole depends on this energy density. Here, we consider the observed frequency f_o .

$$\bar{\Omega}_{AGWB}(f_o) = \frac{d\rho_{GW}}{df} \quad (2.45)$$

The energy density parameter is the frequency-dependent monopole integrated over the logarithmic frequency.

$$\Omega_{GW} = \int d \ln f \Omega_{GW}(f_o) \quad (2.46)$$

$$\approx \int d \ln f \bar{\Omega}_{AGWB}(f_o) \quad (2.47)$$

2.2.1 Astrophysical

GW can be created by different sources. Considering astrophysical sources, they can come from merging binaries, bursts (e.g. from core-collapse supernovae) or continuous waves (e.g. from pulsars). The AGWB consists mostly of compact object mergers, which are mainly black holes and neutron stars.

The current GW detectors like LIGO, Virgo and KAGRA (LVK) have not detected a GW background yet, but they have set upper limits from their third observing run. Assuming a GW energy density parameter proportional to $f^{-2/3}$, which is the case in the inspiral phase of binary black holes Phinney 2001, they arrive at the following integrated energy density.

$$\Omega_{2/3,LIGO} = (3.4 \pm 6.1) \cdot 10^{-9} \quad (2.48)$$

This is compatible with zero, but an anisotropic background would indicate a more interesting cosmology, which is why it would be important to disentangle any anisotropic that could be observed.

The AGWB was detected for the first time this year (2023) using the pulsar time array NANOGrav Agazie et al. 2023. Pulsar time arrays use the fact that pulsars are very accurate clocks. They are rotating neutron stars that have a strong magnetic field and thus emit radio waves in very regular intervals. Since they are so stable, we can use these signals as accurate clocks. If there are any changes in the time of arrival of multiple pulsars, this could indicate a GW background. The NANOGrav experiment used a frequency range of $10^{-8.75} - 10^{-7.5}$ Hz. Also assuming a frequency power law of $f^{-2/3}$, they find the following integrated energy density.

$$\Omega_{2/3,NANOGrav} = 9.3^{+5.8}_{-4.0} \cdot 10^{-9} \quad (2.49)$$

This is higher than the upper limit from LVK, but we have to keep in mind that the analysed frequency range is different for both experiments.

Binary Black Hole Mergers

A compact binary coalescence will produce a chirp-like GW signal, like in 2.3. Both massive objects attract each other and decrease their orbit around each other in the inspiral phase. The potential energy is converted into a GW. After the inspiral phase, the merger and ringdown phases follow, where the new BH becomes axisymmetric and stops emitting GW. The frequency increases over time during all three phases.

The inspiral phase is the simplest to describe analytically, see 2.1. However, in this work, we consider all three phases of the GW. We will see later that this is necessary to derive a frequency dependence.

In this work, we focus on binary black holes. Since most resolved events from LIGO/Virgo are binary black holes. In a recent analysis of the Gravitational Wave Transient Catalogue 3 (GWTC-3) by Collaboration et al. 2022, they considered events with a false alarm rate of less than $\frac{1}{4}$ per year. Out of this sample of 67 events, 63 came from binary black holes, 2 from binary neutron stars and 2 from neutron star-black hole mergers.

If we consider the energy density parameter of the stochastic GW background, we see that binary black holes are present at frequencies up to around 1000 Hz, see Fig. 2.2.

In this figure, all three curves are normalised to the local merger rate from the advanced LIGO/Virgo detectors. Without this normalisation binary BH mergers dominate at most frequencies at which they are present. We can see that for the frequency range of 1 – 1000Hz, it is reasonable to only consider BBH in our analysis

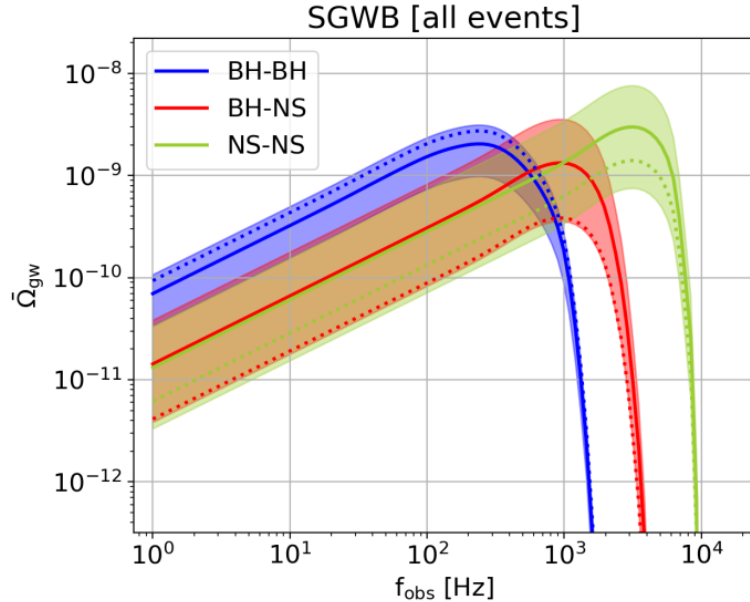


Figure 2.2: The GW energy density parameter as a function of frequency from 1 to 10,000 Hz. This shows the different contributions from BH-BH, NS-NS and BH-NS events. All curves are normalised to the local advanced LIGO/Virgo merger rate. The Figure is taken from Ref. Capurri et al. 2021.

since they are the most present source. However, the applied formalism for the frequency dependence can be generalised to a system of a BH and a neutron star or a system of two neutron stars.

From the waveform, we can extrapolate black hole properties, like the chirp mass and the spin.

$$\mathcal{M}_c = \frac{(m_1 m_2)^{3/5}}{(m_1 + m_2)^{1/5}} \quad (2.50)$$

The frequency is determined by the total mass. The waveform can be decomposed into harmonic, where the quadrupole ($(\ell, m) = (2, 2)$) is naturally the dominant one. (insert from Bonn lectures?)

Dipole

The cosmological principle says, that the universe is isotropic and homogeneous on large scales. GW are one mode of testing this further. If we find anisotropies in the GW background, other than the kinematic dipole and shot noise, this would be evidence against the principle. The kinematic dipole arises from the observer motion with respect to the large-scale structure rest frame. More GW events should be detected in the direction in which we move, and fewer in the opposite direction. Shot noise comes from stochastic fluctuations in the background, which follow a Poisson distribution.

The GW density contrast can be written with an integration over the window function, which weights the contributions in the redshift domain.

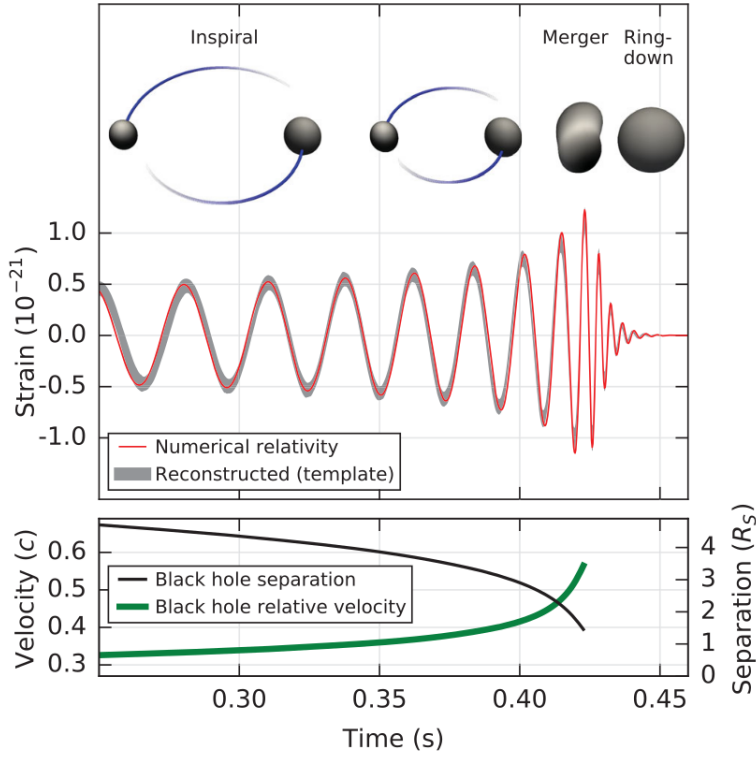


Figure 2.3: The different stages of a BBH merger with the corresponding waveform, here an illustrative estimate of GW150914. The Figure is taken from Ref. Abbott et al. 2016.

$$\delta(f_0, \hat{n}) = \frac{\Omega(f_0, \hat{n}) - \bar{\Omega}(f_0)}{\bar{\Omega}(f_0)} \quad (2.51)$$

$$= \int dz W(f_0, z) \Delta(f_0, \hat{n}, z) \quad (2.52)$$

2.2.2 Cosmological

The major contributions to the cosmological GW background are primordial black holes and GW from phase transitions and inflation. Schulze et al. Schulze et al. 2023 computed the angular power spectrum of this background using a modified version of CLASS Blas, Lesgourgues, and Tram 2011 called `GW_CLASS`. Bubbles of a phase can form in a universe which is in an older phase. In there, magnetohydrodynamic (MHD) turbulence can also produce GW. TODO: PBH shortly Using this code, one can choose a source of this background and compute the associated angular power spectrum. Here, we use the signal from the expected inflationary GW background with a blue tilt. So, we will have a stronger background at higher frequencies compared to lower frequencies.

Inflation

A period of inflation in the early universe solves two important cosmological problems, namely the flatness and the horizon problem. The flatness problem arises when we assume radiation domination followed by matter domination which is followed by Λ (the cosmological constant) domination. The spatial curvature density parameter is measured to be very low.

$$|\Omega_k| = \frac{\rho_k^{\text{eff}}}{\rho_{\text{crit}}} < 10^{-2} \quad (2.53)$$

On the other hand, the radiation energy density parameter is of an even lower order.

$$|\Omega_r| = \frac{\rho_r}{\rho_{\text{crit}}} \in \mathcal{O}(10^{-4}) \quad (2.54)$$

Now the effective curvature energy density ρ_k^{eff} scales like a^{-2} , while the radiation energy density ρ_r scales like a^{-4} , with the scale factor a . At the Planck time $t_P = \sqrt{\frac{\hbar G}{c^5}}$ the ratio between them was many orders of magnitudes lower than 1.

$$\frac{|\rho_k^{\text{eff}}(t_P)|}{\rho_r(t_P)} \approx 10^{-62} \quad (2.55)$$

This seems unlikely since we would expect roughly the same order of magnitude for all the energy density parameters ρ_m , ρ_r , ρ_Λ , and ρ_k^{eff} . Random initial conditions would lead us to the same order of magnitude of these parameters. We also know how Ω_k scales with the scale factor.

$$\Omega_k = -\frac{k}{(aH)^2} = -\frac{k}{\dot{a}^2} \quad (2.56)$$

In the case of an inflationary GW background, the tensor power spectrum $< s(k)$ creates the GW. This is linearly related to the average GW energy density parameter (or monopole) Schulze et al. 2023.

$$\bar{\Omega}_{GW} = \frac{1}{12H_0^2 a_0^2} \frac{\eta_{eq}^2}{2\eta_0^4} P_T(k) \quad (2.57)$$

The GW created through large-scale perturbations during inflation are relevant for wavenumbers $k = 10^{-5} Mpc^{-1} - 1 Mpc^{-1}$, which corresponds to millihertz up to the Hertz range, going through both the sensitivity range of ground-based detectors, like ET Alonso et al. 2020, and space-based detectors like LISA Robson, Cornish, and Liu 2019.

2.2.3 Number Density Distribution

Here, we use the `Multi_CLASS` code, an extension of the `CLASS` code by Bellomo et al. 2020. It was written to adapt the Einstein-Boltzmann solver to gravitational waves. In the computation of the source functions (section 2.2.4), it omits the Limber approximation. This approximation simplifies spherical Bessel functions as Dirac distributions. The spherical Bessel functions are related to the ordinary Bessel functions

in the following way.

$$j_n(x) = \sqrt{\frac{\pi}{2x}} J_{n+1/2}(x) \quad (2.58)$$

The ordinary Bessel functions are defined with the gamma function.

$$J_n(x) = \sum_{m=0}^{\infty} \frac{(-1)^m}{m! \Gamma(m+n+1)} \left(\frac{x}{2}\right)^{2m+n} \quad (2.59)$$

The `Multi_CLASS` code uses the number density of detectable GW per redshift per solid angle element from Scelfo et al. 2018:

$$\frac{d^2 N_{GW}}{dz d\Omega} = T_{obs} \frac{c\chi^2(z)}{(1+z)H(z)} R_{tot}(z) F_{GW}^{detectable}(z). \quad (2.60)$$

T_{obs} is the total observational time, $\chi(z)$ is the comoving distance, $H(z)$ is the Hubble rate, $R_{tot}(z)$ is the total comoving merger rate and $F_{GW}^{detectable}(z)$ the fraction of detectable events. For the merger rate, they include primordial BH and BBH in their calculation. The authors choose the common SNR threshold $\langle \rho^2 \rangle = 8$.

$$\langle \rho^2 \rangle = \frac{1}{5} \int_{f_{min}}^{f_{max}} df \frac{h_c^2(f)}{f^2 S_n(f)} \quad (2.61)$$

For the Einstein Telescope (ET), they find that $F_{GW}^{detectable} \approx 1$ even for redshifts above 5, which have a small effect on the detection overall.

2.2.4 Projection Effects

change style, explain physics-> papers Yoo, Bonvin

For the intrinsic anisotropies, there are different contributions to the source functions Δ_l^{AGWB} . The different pertinent effects are density fluctuations, redshift space distortions, the Doppler effect and relativistic corrections or gravitational potential terms. Di Dio et al. 2013.

We write each random field as a product of the primordial curvature perturbation and a transfer function. In Dall’Armi, Ricciardone, and Bertacca 2022, they compute the different source terms using the `CLASSgal` framework. The implementation in `CLASS` follows the same framework, since `CLASSgal` has been merged into the standard public code.

$$X(\eta, \vec{k}) = T_X(\eta, \vec{k}) \zeta(\vec{k}) \quad (2.62)$$

The two-point correlation function of the curvature perturbation has the following form.

$$\langle \zeta(\vec{k}) \zeta * (\vec{k}') \rangle = (2\pi)^3 \delta(\vec{k} - \vec{k}') \frac{2\pi^2}{k^3} P(k) \quad (2.63)$$

There is one density source term, dependent on the transfer functions of matter density fluctuations $T_{\delta m}$ and of the velocity divergence of matter $T_{\theta m}$. Here, $\bar{\chi}$ is a shifted conformal time variable.

$$\bar{\chi} = \eta_0 - \eta \quad (2.64)$$

$$\Delta_\ell^{den} = \int_0^{\eta_0} d\eta W \left(bT_{\delta m} + 3\frac{aH}{k^2} T_{\theta_m} \right) j_l(k\bar{\chi}) \quad (2.65)$$

Here, $j_l(k\bar{\chi})$ is the spherical Bessel function and we integrate over conformal time using the window function, like in the following source contributions.

The Doppler terms also depend on the velocity divergence of matter since the velocity determines the Doppler effect.

$$\Delta_\ell^{D1} = \int_0^{\eta_0} d\eta W \frac{T_{\theta_m}}{k} \left(-b_e + \frac{H'}{aH^2} + 3 \right) \frac{d}{d(k\bar{\chi})} j_l(k\bar{\chi}) \quad (2.66)$$

$$\Delta_\ell^{D2} = \int_0^{\eta_0} d\eta W T_{\theta_m} (b_e - 3) \frac{aH}{k^2} j_l(k\bar{\chi}) \quad (2.67)$$

The term for the redshift space distortions was derived by Kaiser 1987 and depends on the second derivative of the bessel function.

$$\Delta_\ell^{RSD} = \int_0^{\eta_0} d\eta W T_{\theta_m} \frac{1}{aH} \frac{d^2}{d(k\bar{\chi})^2} j_l(k\bar{\chi}) \quad (2.68)$$

There are five relativistic corrections, which can also be called gravitational potential terms since the redshift space distortions are also relativistic. In the GW case, two of these terms vanish (Dall'Armi, Ricciardone, and Bertacca 2022), while the other three are non-zero.

$$\Delta_\ell^{G1} = \int_0^{\eta_0} d\eta W T_\Psi \left(4 - b_e + \frac{H}{aH^2} \right) j_l(k\bar{\chi}) \quad (2.69)$$

$$\Delta_\ell^{G3} = \int_0^{\eta_0} d\eta W T_{\Phi'} \frac{1}{aH} j_l(k\bar{\chi}) \quad (2.70)$$

$$\Delta_\ell^{G5} = \int_0^{\eta_0} d\eta W \left(-b_e + \frac{H'}{aH^2} + 3 \right) \int_0^{\tilde{\eta}} d\tilde{\eta} j_l(k\bar{\chi}) \left(T_{\Phi'}(\tilde{\eta}) T_{\Psi'}(\tilde{\eta}) - \frac{1}{2} T'_{h,ij}(\tilde{\eta}) n^i n^j \right) \quad (2.71)$$

In the last equation, n^i are the components of the line of sight vector.

$$\delta_{AGWB}(f_0, \hat{n}) = \int dz \tilde{W}(f_0, z) \Delta_{AGWB}(f_0, \hat{n}, z) \quad (2.72)$$

$$\begin{aligned} &= \int d\bar{\chi} \tilde{W} [b(\delta_m - 3\mathcal{H}V) + (3 - b_e)\mathcal{H}V + \Psi(3 - b_e + \frac{\mathcal{H}'}{\mathcal{H}^2}) + 2I(b_e - \frac{\mathcal{H}'}{\mathcal{H}^2} - 2) \\ &\quad + (\delta a_0 + \Psi_0 - v_{\parallel 0})(b_e - \frac{\mathcal{H}'}{\mathcal{H}^2} - 2) - v_{\parallel}(-b_e + \frac{\mathcal{H}'}{\mathcal{H}^2} + 2) \\ &\quad + \frac{1}{\mathcal{H}}\Phi' - \frac{1}{\mathcal{H}}\partial_{\parallel}v_{\parallel} - \frac{1}{2\mathcal{H}}h'^{TT}_{ij}n^i n^j] \end{aligned} \quad (2.73)$$

Here the following notation is used:

$$v_{\parallel} = \hat{n}\vec{v} \quad (2.74)$$

$$\partial_{\parallel} = \hat{n}\vec{\nabla} \quad (2.75)$$

$$I(\tilde{\chi}) = -\frac{1}{2} \int_0^{\bar{x}} d\tilde{\chi} (\Psi' + \Phi' - \frac{1}{2} h'_{ij})(\tilde{\chi}) \quad (2.76)$$

$$\vec{v} = \vec{\nabla} V \quad (2.77)$$

3

Frequency Dependence of the AGWB

The AGWB is not independent of the observed frequency of the GW. In the standard `Multi_CLASS` code, it is possible to compute the angular power spectrum of the AGWB. However, this does not include any frequency dependency of this background which can generally not be neglected, see Dall’Armi, Ricciardone, and Bertacca 2022. Therefore I added this frequency dependency which enters in two instances here. One is the frequency-dependent window function that weights contributions from different redshifts and the second is the evolution bias which accounts for new sources being added with time (i.e. lower z). Both will be discussed in section 3.5 and 3.7.

We need to specify the GW frequency as a parameter in the initialisation file that we give to CLASS, so we implemented it as a new input parameter for `Multi_CLASS`.

As we can see in Dall’Armi, Ricciardone, and Bertacca 2022 the window function and the evolution bias depend on the frequency. But this is only the case if we consider not only the inspiral phase but also the merger and ringdown phases. For the inspiral phase we would have the following energy spectrum.

$$\frac{dE_{GW}}{df_e d\Omega_e} \propto f_0^{-\frac{1}{3}} (1+z)^{-\frac{1}{3}}. \quad (3.1)$$

$$\bar{\Omega}_{AGWB} \propto f_0^{\frac{2}{3}} \quad (3.2)$$

Considering only the inspiral phase would then make the window function frequency independent.

$$\tilde{W}(z) \propto \frac{f_0(E_{GW}/df_e)}{\bar{\Omega}_{AGWB}(f_0)} = const. \quad (3.3)$$

For that reason, it is necessary to consider all three phases of the merger which we will see in the energy spectrum.

3.1 Energy Spectrum

For the modelling of all three phases we can use the waveform by Ajith et al. 2011.

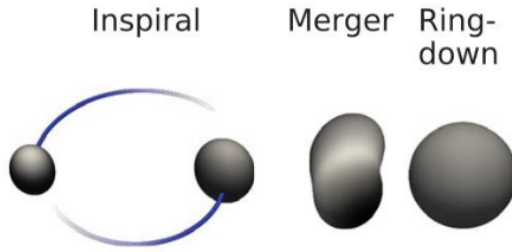


Figure 3.1: The three phases of a binary coalescence: inspiral, merger and ringdown.

$$A(f) = Cf_1^{-7/6} \begin{cases} f'^{-7/6}(1 + \sum_{i=2}^3 \alpha_i v^i) & f < f_1 \\ \omega_m f'^{-2/3}(1 + \sum_{i=1}^2 \epsilon_i v^i) & f_1 \leq f < f_2 \\ \omega_r \mathcal{L}(f, f_2, \sigma) & f_2 \leq f < f_3 \end{cases}$$

Note that this is the amplitude as a function of the frequency, so a Fourier transform of $A(t)$.

$$A(f) = \frac{1}{\sqrt{2\pi}} \int_{\mathbb{R}} A(t) e^{-ift} dt \quad (3.4)$$

The parameters ω_m and ω_r are used to make the function continuous. For the ringdown, we have a Lorentzian function centred around the merger to ringdown transition frequency f_2 with the width σ . The parameters α_i are post-Newtonian corrections.

Parameter	α_2	α_3	ϵ_1	ϵ_2
Value	$-323/224 + 451\eta/168$	$(27/8 - 11\eta/6)\chi$	$1.455\chi - 1.890$	$-1.815\chi + 1.656$
No Spin	$-323/224 + 451\eta/168$	0	-1.890	1.656

Table 3.1: Amplitude parameters with and without the zero spin approximation.

The frequency f_1 at the transition of the inspiral and merger phase is the last stable orbit of the binary. Once the merger phase has started the orbits cease to be stable since the objects start to fall in. This frequency was calculated by Bardeen, Press, and Teukolsky 1972.

$$f_1 = \frac{c^3}{6^{3/2} 2\pi M_{tot} G} \quad (3.5)$$

The transition frequency from merger to ringdown is given by the least-damped mode (Maggiore 2008) which is also the dominant quasi-normal mode. This is part of the description of the BBH system as characterised by n normal modes with frequencies ω_n , discussed further in chapter 12.3 of the same book.

$$f_2 \approx 0.747 \frac{c}{2\pi R_S} \approx 12 \text{kHz} \left(\frac{M_{\odot}}{M} \right) \quad (3.6)$$

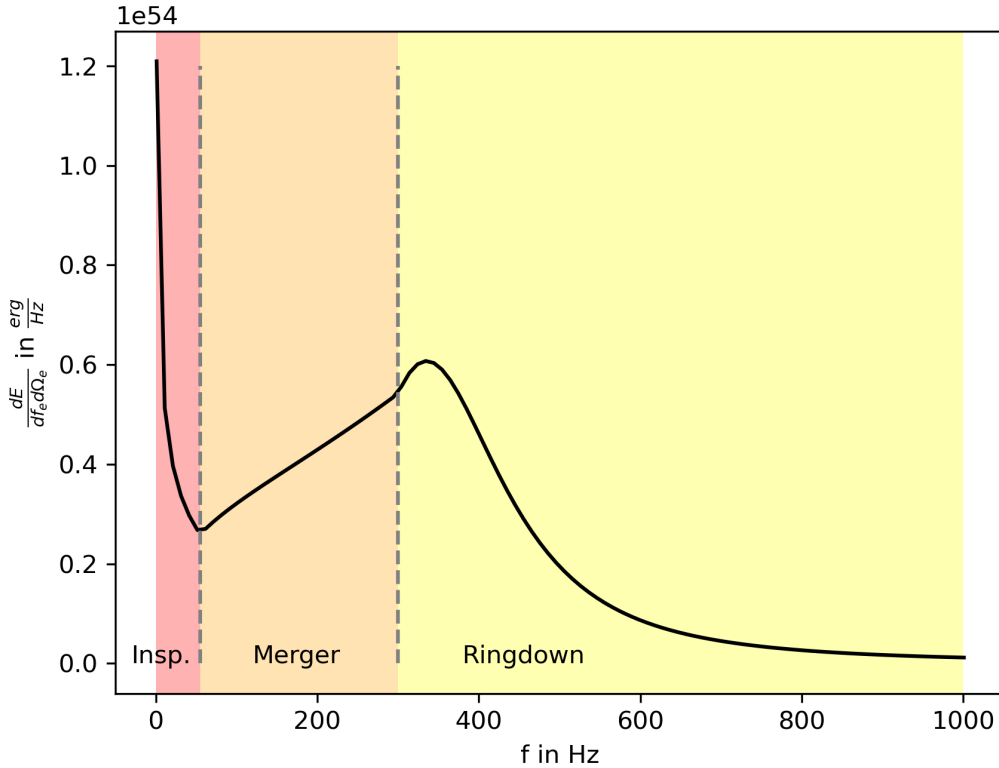


Figure 3.2: The energy spectrum as a function of frequency for a BBH merger where both BH have a mass of $20M_\odot$.

Later, we will consider the square strain as a function of frequency $|h(f)|^2$ for the energy spectrum, so we can ignore the phase $\psi(f)$.

$$h(f) = A(f)e^{-i\psi(f)} \quad (3.7)$$

Here the redshift dependence will come in through the derivation by the emission frequency, see e.g. 3.39. From this waveform template, we can get the energy spectrum in the following way.

$$\frac{dE_{GW,e}}{df_e d\Omega_e} = \frac{\pi d_L^2 c^3 f_o^2}{2G(1+z)^2} |h(f_o)|^2 \propto f_o^2 h^2(f_o) \propto h^2(t) \quad (3.8)$$

If we plot the energy spectrum as a function of z for different frequencies, see Fig. 3.3, we can see different sections of Fig. 3.2. This is because $d^2E_{GW,e}/df_e d\Omega_e$ only depends on z through the emitted frequency. The energy spectrum is written as a function of f_e , but we implement it in such a way that the user can choose the received frequency at the detector.

$$f_e = (1+z)f_0 \quad (3.9)$$

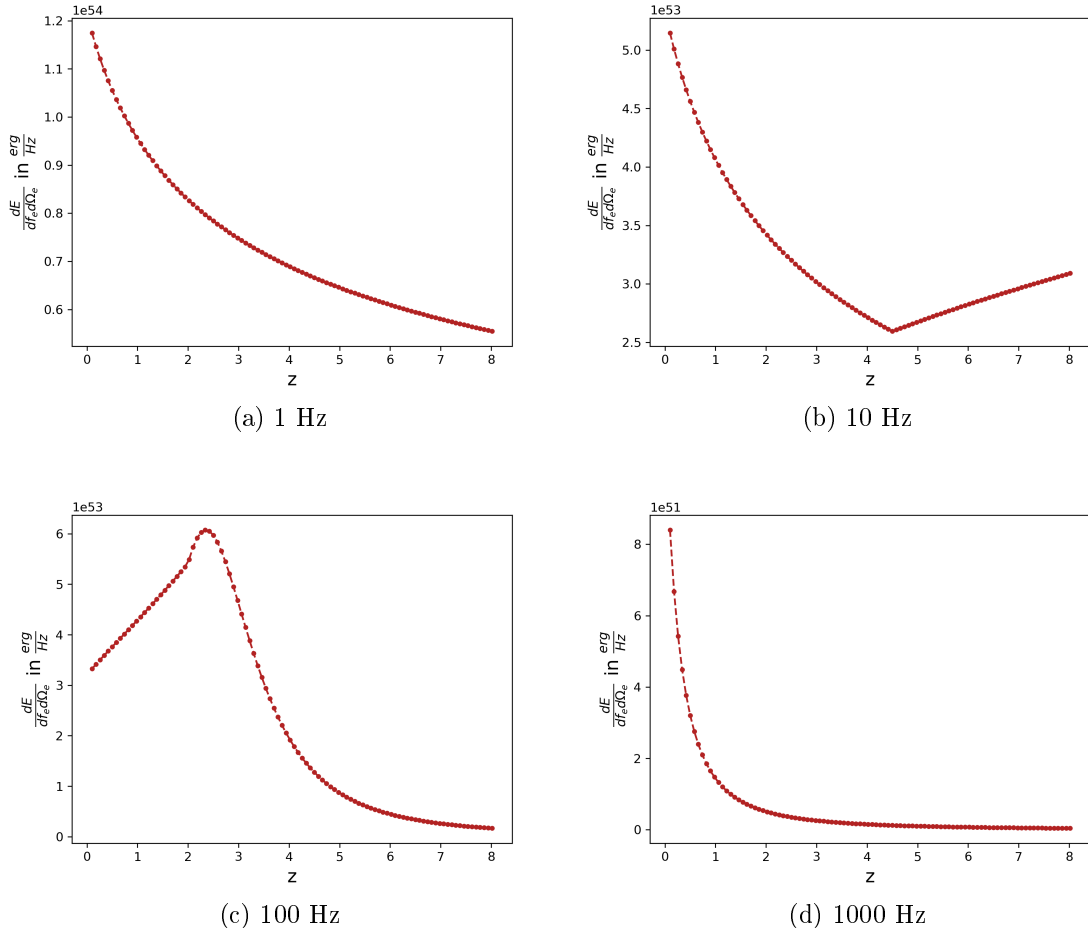


Figure 3.3: The energy spectrum $d^2E_{GW,e}/df_e d\Omega_e$ at different observed frequencies as a function of redshift.

3.2 Star Formation Rate

The BBH merger rate depends on the star formation rate (SFR) which is the rate at which gas and dust are turned into stars. This is relevant since BH are end products of stellar evolution.

$$R_{BBH}(z) \propto \int dM_h \frac{dn}{dM_h}(z_f, M_h) \langle SFR(M_h, z_f) \rangle_{SF} \quad (3.10)$$

For the star formation rate, we use the UNIVERSEMACHINE code from Behroozi et al. 2019. They use observational constraints and data from simulations to compute SFR for individual galaxies.

In the Λ CDM cosmology, galaxies form at the centre of haloes. Haloes are gravitationally self-bound structures that contain virialised dark matter. This means that the virial equation applies in this case. Here, T is the potential energy and U is the kinetic energy.

$$2T = U \quad (3.11)$$

So far, there exists no framework in which we can derive the SFR from first principles. This is why the authors use a double power law plus Gaussian and determine the best-fit parameters for this functional form. This determines the SFR for every halo at a given redshift. They use weak priors and observational constraints for less bias and the potential to reveal new physics.

Dark matter simulations, here Bolshoi-Planck [A. A. Klypin, Trujillo-Gomez, and Primack 2011] and MultiDark Planck 2 (MDPL2) A. Klypin et al. 2016, are used, which simulate a mock universe. They contain halo merger trees, which can be compared to observations. Behroozi et al. used data from multiple experiments, such as the Sloan Digital Sky Survey (SDSS) Abazajian et al. 2009, Ultravista McCracken et al. 2012. The observables include stellar mass functions, UV luminosity functions and galaxy auto-correlation functions. Using this data, they compute a likelihood and run a Markov Chain Monte Carlo (MCMC) algorithm to sample the SFR range.

Like in Dall’Armi, Ricciardone, and Bertacca 2022 we consider only star-forming galaxies. This could be modified in a future version of the code by including the fraction of quenched galaxies $f_Q = 1 - f_{SF}$, which could be taken from the UNIVERSEMACHINE paper as well. The adopted SFR functional form is the following. The fit parameters depend on the rotational velocity at peak halo mass v_{Mpeak} and on the redshift. This velocity only depends on the halo mass M_h , see below.

$$\langle SFR_{SF}(M_{peak}(v_{Mpeak,z}), z) \rangle = \epsilon \left[(v^\alpha + v^\beta)^{-1} + \gamma \exp\left(-\frac{\log_{10}(v)^2}{2\delta^2}\right) \right] \quad (3.12)$$

The characteristic SFR in $M_\odot \text{ yr}^{-1}$ is the global factor ϵ . For the slope of the $SFR - v_{Mpeak}$ relation, we have a faint-end and a massive-end slope parameter α and β , respectively. This is because $v_{Mpeak} \propto M_h^3$ 3.20, so a higher velocity at the peak mass corresponds to a higher halo mass. Furthermore, γ is the strength and δ the width of the Gaussian SFR efficiency boost.

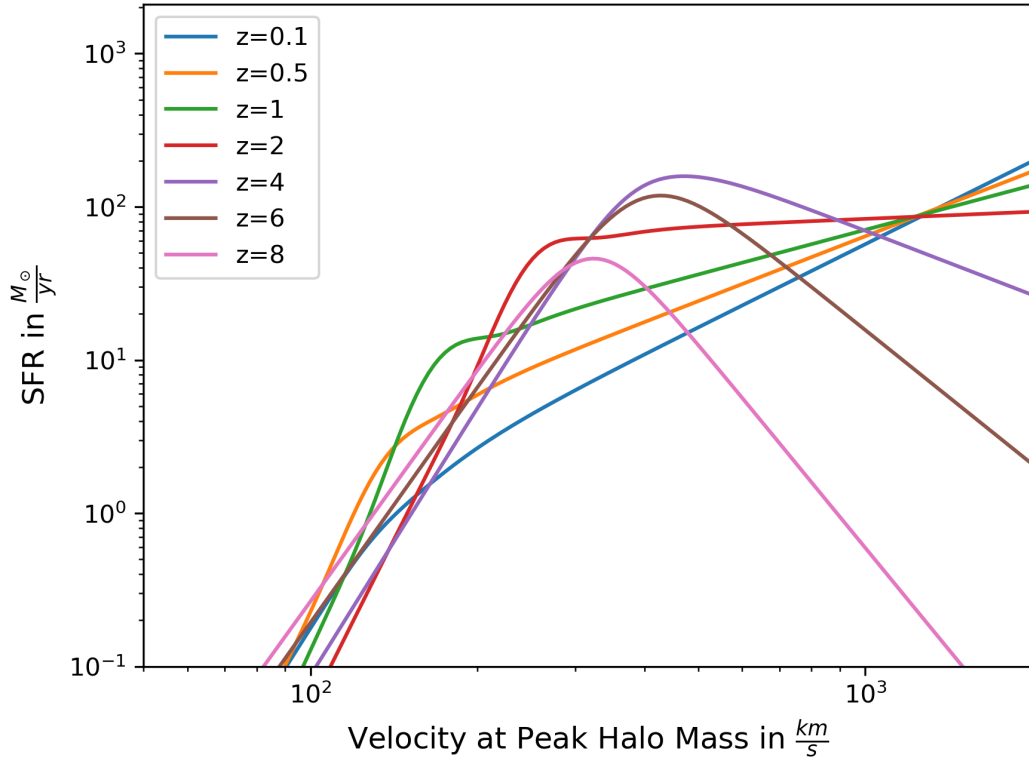


Figure 3.4: The SFR for star-forming galaxies for different redshifts. The velocity at the historical peak halo mass corresponds to the standard halo mass, see equation 3.20.

The velocity v is defined as the ratio of the real (v_{Mpeak}) and the characteristic (V) velocity at the halo peak mass, both in km s^{-1} .

$$v = \frac{v_{Mpeak}}{V \cdot \text{km s}^{-1}} \quad (3.13)$$

The other parameters, except for δ , scale differently for different redshift regions. For V , ϵ and α , the scaling is separated into $z = 0$, $z \approx 1 - 2$, $z = 3 - 7$ and $z > 7$. The parameters β and γ have three scaling regions instead of four, as they are not well constrained at high redshifts.

$$\log_{10}(V) = V_0 + V_a(1 - a) + V_{la}\ln(1 + z) + V_z z \quad (3.14)$$

$$\log_{10}(\epsilon) = \epsilon_0 + \epsilon_a(1 - a) + \epsilon_{la}\ln(1 + z) + \epsilon_z z \quad (3.15)$$

$$\alpha = \alpha_0 + \alpha_a(1 - a) + \alpha_{la}\ln(1 + z) + \alpha_z z \quad (3.16)$$

$$\beta = \beta_0 + \beta_a(1 - a) + \beta_z z \quad (3.17)$$

$$\log_{10}(\gamma) = \gamma_0 + \gamma_a(1 - a) + \gamma_{la}\ln(1 + z) + \gamma_z z \quad (3.18)$$

$$\delta = \delta_0 \quad (3.19)$$

The median v_{Mpeak} is taken from the *Bolshoi-Planck* DM simulation as

$$v_{Mpeak}(M_h, a) = 200 \frac{km}{s} \left[\frac{M_h}{M_{200kms}(a)} \right]^3 \quad (3.20)$$

$$M_{200kms}(a) = \frac{1.64 \cdot 10^{12} M_\odot}{\left(\frac{a}{0.378} \right)^{-0.142} + \left(\frac{a}{0.378} \right)^{-1.79}}. \quad (3.21)$$

3.3 Halo Mass Function

The merger rate of BBH depends on the number of haloes since their formation takes place in haloes. This is why it depends on the halo mass function (HMF) $\frac{dn}{dM_h}(z_f, M_h)$ integrated over the halo mass.

$$R_{BBH}(z) \propto \int dM_h \frac{dn}{dM_h}(z_f, M_h) \langle SFR(M_h, z_f) \rangle_{SF} \quad (3.22)$$

The HMF is the comoving number density of haloes with masses between M and $M + dM$.

We first consider the variance of the matter density field σ^2 which we get from the linear matter power spectrum integrated over the wavenumber k with a window function. This is the Fourier transform of a tophat function in real space with the width R , corresponding to the radius of the spherical halo. Physically, overfull regions in the universe gravitationally attract and form haloes.

$$\sigma^2(R, z) = \int_0^\infty k^2 P_{lin}(k, z) W^2(k, R) dk \quad (3.23)$$

For a spherical halo model, we get the radius through the mass and the density.

$$R = \sqrt[3]{\frac{3M}{4\pi\rho_m}} \quad (3.24)$$

Then, the halo mass function comes from the logarithmic derivative of σ^{-1} by the halo mass.

$$\frac{dn(M)}{dM} = \frac{\rho_m}{M^2} \frac{d \ln(\frac{1}{\sigma})}{d \ln M} f_{NL}(\sigma) \quad (3.25)$$

The factor f_{NL} accounts for non-linear effects in the halo collapse. There are different ways to model these effects. A common analytical one is the Press-Schechter formalism parametrised by the critical overdensity δ_c .

$$\delta = \frac{\delta\rho}{\bar{\rho}} \quad (3.26)$$

$$f_{PS}(\sigma) = \sqrt{\frac{2}{\pi}} \frac{\delta_c}{\sigma} \exp\left(-\frac{\delta_c^2}{2\sigma^2}\right) \quad (3.27)$$

Here, we use the parametrisation by **tinker_toward_2008**. They use a fitting formula depending on the overdensity Δ . The overdensity characterises how much

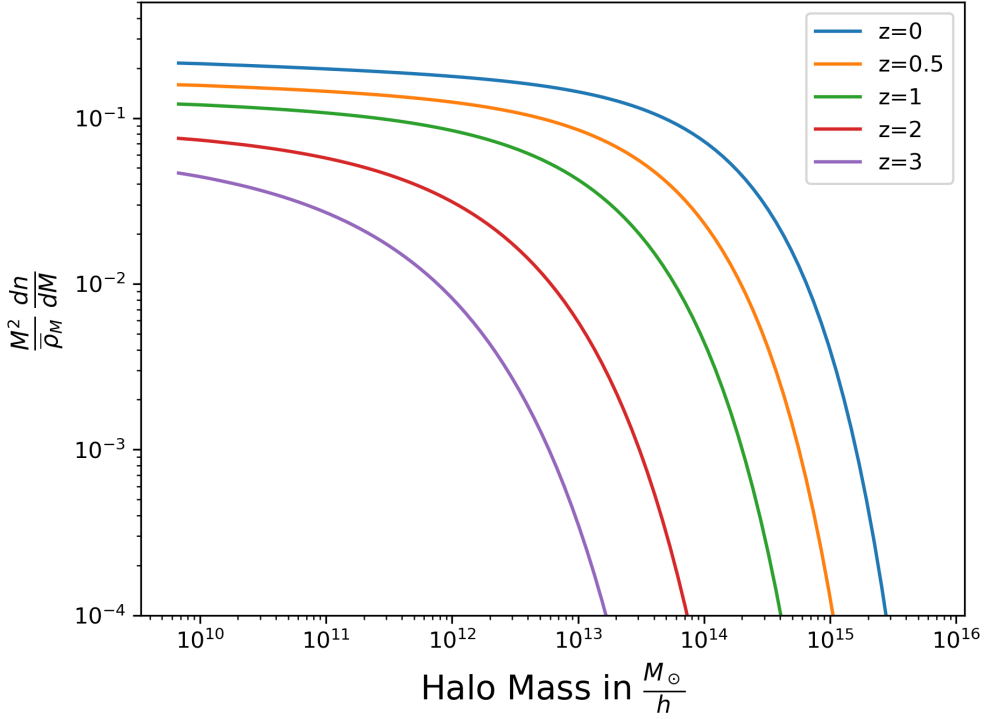


Figure 3.5: The dimensionless HMF for different redshifts z at $\Delta = 800$.

denser the halo is compared to the average universe density $\bar{\rho}_m$ at the corresponding redshift.

$$\Delta = \frac{3M_\Delta}{4\pi R_\Delta^3 \bar{\rho}_m} \quad (3.28)$$

The non-linear corrections then have the following form.

$$f(\sigma) = A \left(\left(\frac{\sigma}{b} \right)^{-a} + 1 \right) \exp\left(-\frac{c}{\sigma^2}\right) \quad (3.29)$$

The used fitting parameters, dependent on the overdensity, are the following.

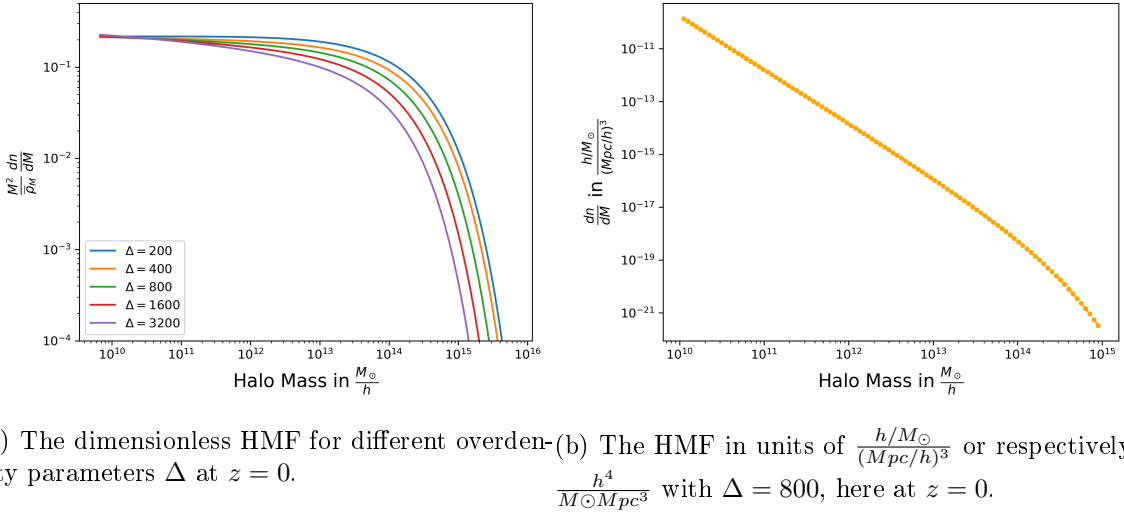
$$A = \begin{cases} 0.1(\log_{10} \Delta) - 0.05 & \Delta < 1600 \\ 0.26 & \Delta \geq 1600 \end{cases}$$

$$a = 1.43 + (\log_{10} \Delta - 2.3)^{1.5} \quad (3.30)$$

$$b = 1.0 + (\log_{10} \Delta - 1.6)^{-1.5} \quad (3.31)$$

$$c = 1.2 + (\log_{10} \Delta - 2.35)^{1.6} \quad (3.32)$$

To show how the redshift and the overdensity influence the HMF, we vary the parameter in Fig. 3.6a.


 Figure 3.6: The HMF at $z = 0$.

3.4 Merger Rate

With the SFR and the HMF, we can now calculate the BBH merger rate.

$$R_{BBH}(z = 0) = 19 \text{ Gpc}^{-3}\text{yr}^{-1} \quad (3.33)$$

$$R_{BBH}(z) = \mathcal{A}_{LIGO}^{BBH} \int dt_d p(t_d) \int dM_h \frac{dn}{dM_h}(z_f, M_h) \langle SFR(M_h, z_f) \rangle_{SF} \quad (3.34)$$

Here, we have the time delay distribution $p(t_d)$, where the time delay takes place between the formation and the merger of the binary.

$$p(t_d) = \ln \left(\frac{t(z)}{t_{d,min}} \right) \frac{1}{t_d} \quad (3.35)$$

The minimum time delay is 50 Myr, like in Dall’Armi, Ricciardone, and Bertacca 2022.

The merger rate is also multiplied by a normalisation factor \mathcal{A}_{LIGO}^{BBH} , corresponding to the local merger rate estimated by LIGO/Virgo (Collaboration et al. 2022).

$$R_{BBH}(0) = 19 \frac{1}{\text{Gpc}^3\text{yr}} \quad (3.36)$$

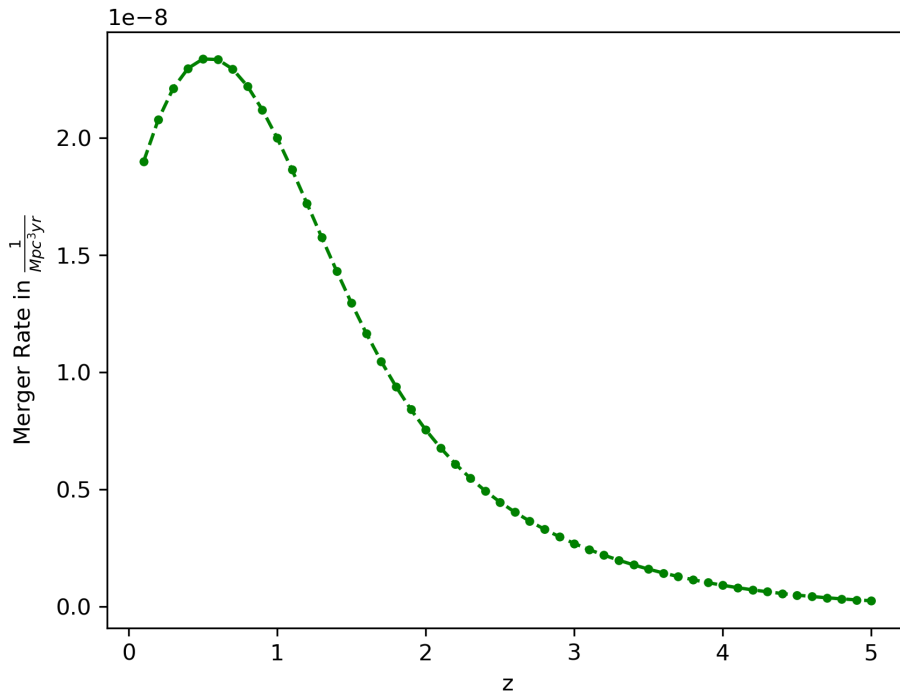


Figure 3.7: The BBH merger rate as a function of the redshift z .

3.5 Window Function

In Dall’Armi et al. Dall’Armi, Ricciardone, and Bertacca 2022 we see that the frequency dependence of the dipole comes from the evolution bias and the window function. The evolution bias accounts for the fact that more sources are created with time. The window function is used when we integrate the source functions over the redshift. It weights different redshift regions of the source functions depending on which ones are important for the observable, in this case GW.

$$\delta_{AGWB}(f_o, \hat{n}) = \frac{\Omega_{AGWB}(f_o, \hat{n}) - \bar{\Omega}_{AGWB}(f_o)}{\bar{\Omega}_{AGWB}(f_o)} \quad (3.37)$$

$$= \int dz \tilde{W}(f_o, z) \Delta_{AGWB}(f_o, \hat{n}, z) \quad (3.38)$$

In the standard version without frequency dependence, we can already see the influence of the different window functions and redshift ranges.

The different window functions are plotted in Fig.3.8. The window function determines which part of our source function we count for the density contrast. In the case of a Dirac distribution, we count all parts and skip the integration. This is why that window function leads to a higher angular power spectrum.

We can see the GW angular power spectrum for different redshifts in Fig.3.9. The anisotropies are higher for smaller redshifts. This is due to the fact that we have more GW sources at lower redshifts due to structure formation growing linearly with

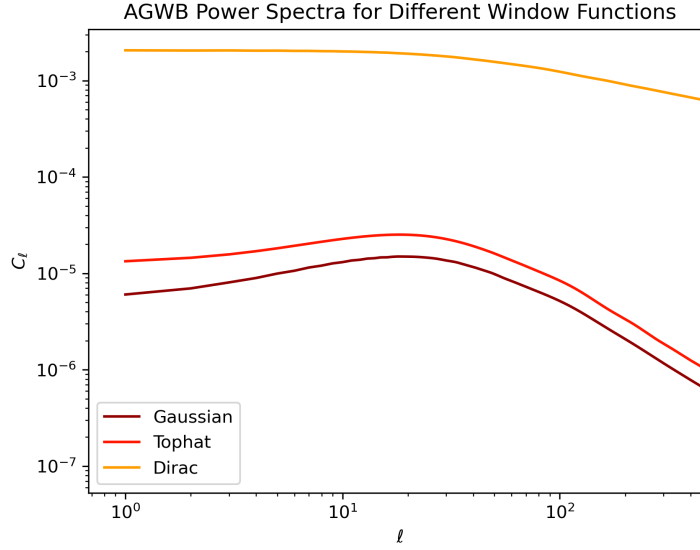


Figure 3.8: GW angular power spectrum for different window functions.

the scale factor a .

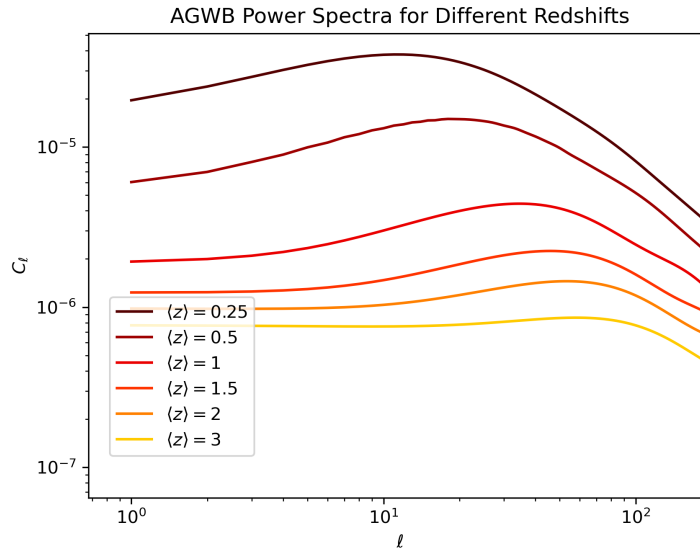


Figure 3.9: GW angular power spectrum for different redshifts.

$$\tilde{W}(z, f_0) = \frac{f_0}{\rho_c c^2 \bar{\Omega}_{AGWB}(f_0)} \frac{R_{BBH}(z)}{(1+z)H(z)} \left. \frac{dE_{GW}}{df_e d\Omega_e}(f_e) \right|_{f_e=(1+z)f_0} \quad (3.39)$$

The window function is normalised using the monopole, which is the same expression integrated over z .

$$\bar{\Omega}_{AGWB}(f_0) = \frac{f_0}{\rho_c} \frac{d\rho_{GW}}{df} \quad (3.40)$$

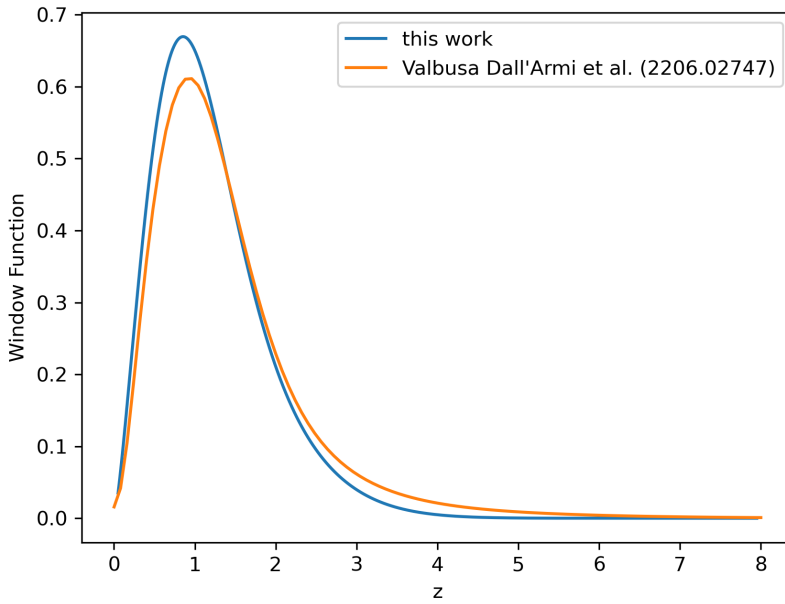


Figure 3.10: The final window function at 1 Hertz for this code in blue for comparison with Dall’Armi, Ricciardone, and Bertacca 2022 in orange.

$$= \frac{f_0}{\rho_c c^2} \int \frac{dz}{(1+z)H(z)} R_{BBH}(z) \frac{dE_{GW}}{df_e d\Omega_e}(f_e) \quad (3.41)$$

We then Fourier and Legendre transform the GW density contrast to get Legendre polynomials corresponding to multipoles on the sphere.

$$\delta_X(f_0, \vec{k}) = \int \frac{d^3 \vec{x}}{(2\pi)^{\frac{3}{2}}} \delta_X(f_0, \vec{x}) \quad (3.42)$$

$$\Delta_l(k, f_0) = \int d\phi \int d\mu \mathcal{P}_l(\mu) \delta(\vec{k}, f_0) \quad (3.43)$$

From that, we can calculate the angular power spectrum using the primordial power spectrum.

$$C_l = 4\pi \int \frac{dk}{k} P(k) \Delta_l \Delta_l^* \quad (3.44)$$

Note, that this Δ is not the same as in equation 2.72.

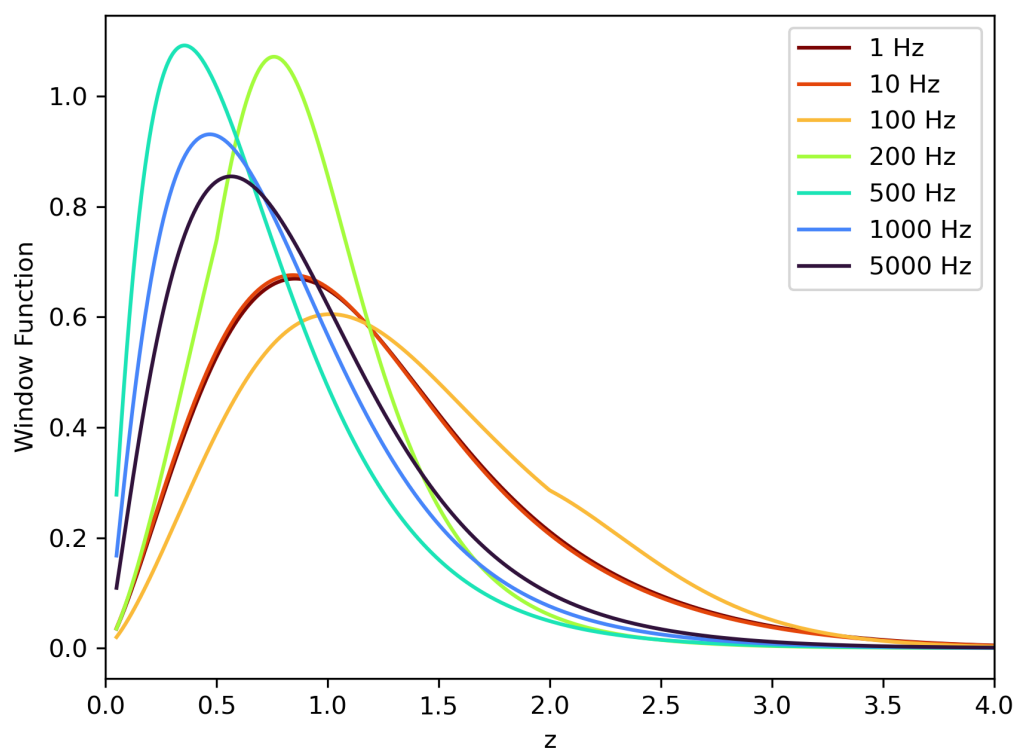


Figure 3.11: The window functions at different observed frequencies.

3.6 Bias & Magnification Bias

If we see GW as a tracer of the underlying dark matter density field, we have to introduce a bias for this tracer, where δ is again the density contrast.

$$\delta_{DM} = b_{GW} \delta_{GW} \quad (3.45)$$

Scelfo et al. 2018 find this bias to be 1.81 considering BH from the end-point of stellar evolution (as opposed to primordial BH).

Another bias we consider is the magnification bias. It accounts for gravitational lensing which increases the area of the source and thus decreases the observed number density. Furthermore, fainter object can reach the magnitude threshold due to gravitational lensing.

If one compares the contributions to Δ_l^{AGWB} between **CLASSgal** and the Dall’Armi paper Dall’Armi, Ricciardone, and Bertacca 2022, the magnification bias has to be $s = \frac{2}{5}$ for the expressions to match. To find out why this is the case, I tried some calculations with $\frac{dN}{dz}$, but could not match this value. After reading the paper by Bertacca et al. Bertacca et al. 2020 (recommended by Lorenzo), one can see that they derive their expressions from first principles without introducing the magnification bias separately.

3.7 Evolution Bias

The evolution bias accounts for the creation of new sources. This is why it depends on the redshift derivative of the merger rate and the energy spectrum of one merger. It enters in the projection effects in section 2.2.4. We can write this in terms of the derivative of the GW energy flux of the scale factor a .

$$b_e(f_0, z) = \frac{d \ln(F)}{d \ln(a)}(f_0, z) \quad (3.46)$$

$$= -\frac{1+z}{F(f_0, z)} \frac{dF}{dz}(f_0, z) \quad (3.47)$$

The energy flux of GW is a product of the energy spectrum of one binary, using the waveform by Ajith et al. Ajith et al. 2011 and the merger rate of binary black holes as a function of redshift.

$$F(f_0, z) = R_{BBH}(z) \frac{dE_{GW}}{df_e d\Omega_e}(f_0, z) \quad (3.48)$$

In Fig.3.12, we show the computed angular power spectrum with and without the evolution bias. We can see that it barely influences the overall power spectrum. Computationally, it takes much longer to consider it since the merger rate and energy spectrum are computed again at every step. The merger rate for example contains an integral over the halo mass which increases the runtime. Because of this minor influence, we neglect the evolution when computing the angular power spectra, but it can easily be activated and deactivated in the `Multi_CLASS` initialisation file

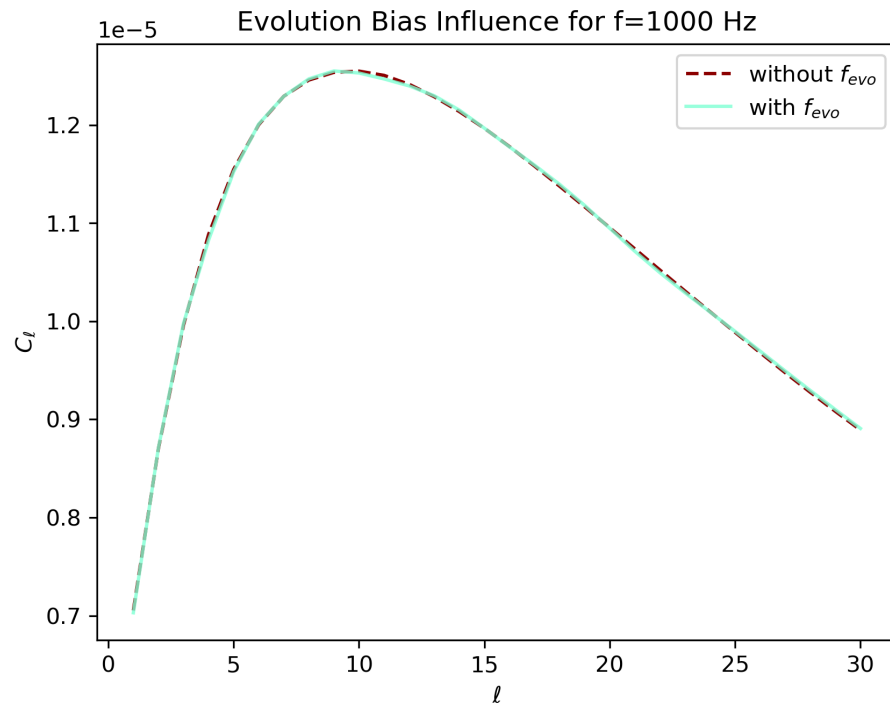


Figure 3.12: The influence of the evolution bias on the angular power spectrum at an observed frequency of 1000 Hertz.

(`disable_gw_evo_bias`).

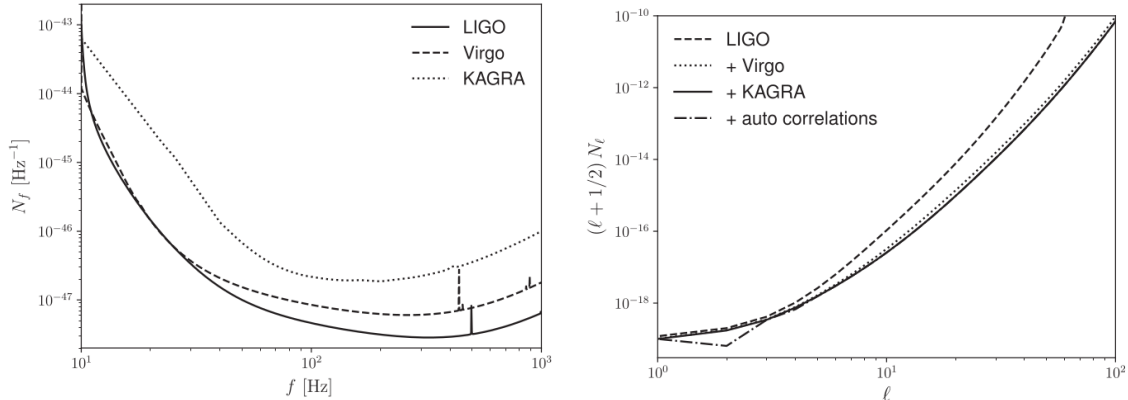
4

Instrumental Noise

Currently, the main problem in extracting the GW background is the high instrumental noise. Ground-based detectors today, like LIGO, Virgo & KAGRA are not able to detect any GW background as discussed in section 2.2.1. This is why we need future detectors such as Einstein Telescope (ET) or Cosmic Explorer (CE) to achieve a higher sensitivity.

4.1 LIGO, Virgo & KAGRA

The current most sensitive GW observatory is LIGO in the United States, operating an interferometer with two arms, each 4 km long. The data is analysed jointly with the Virgo detector in Italy and KAGRA in Japan. This is very useful since it allows cross-correlation which lowers the noise level.



(a) Noise sensitivity with respect to frequency for LVK.
(b) The noise angular power spectrum for LVK.

Figure 4.1: Design sensitivity curves for the LVK detector network. For LIGO, this is the advanced LIGO A+ design sensitivity and for Virgo the O5 sensitivity. This figure is taken from Alonso et al. 2020.

In Fig. 4.1a, we see how the sensitivity changes with respect to the frequency. The most sensitive frequency range is at 100–1000 Hertz. The noise power spectrum

in Fig. 4.1 tells us at which magnitude we could expect to measure a certain multipole. As can be seen in Fig. 4.1b, using cross-correlations between the ground-based detectors improves the sensitivity, especially at higher multipoles. Adding auto-correlations of the detectors mostly influences $\ell = 2$, which is due to the L-shaped geometry of the detectors.

4.2 Einstein Telescope & Cosmic Explorer

ET will be a third-generation ground-based observatory, built either in the Limburg region in the Netherlands or in Sardinia in Italy. Its sensitivity will be vastly improved compared to LVK. This is due to the fact that it will operate in three arms with 10 km each instead of two arms measuring 4 km like LVK. A similar project is planned in the United States, called Cosmic Explorer (CE). It will have two arms with an unprecedented length of 40 km. The frequency sensitivity curves are shown in Fig. 4.2.

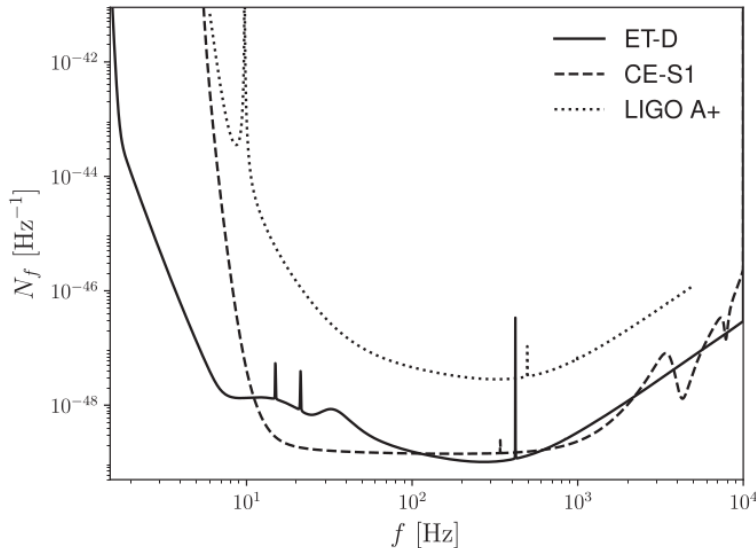


Figure 4.2: The design sensitivity curve for ET and CE compared to LIGO A+. This figure is taken from Alonso et al. 2020.

ET and CE in cross-correlation will improve the sensitivity in the angular power spectrum by around 4 orders of magnitude, see Fig. 4.3. Here again, the improvement coming from the auto-correlation at $l = 2, 4$ is due to the detector shape.

Using the cross-correlations between ET and CE, see Fig. 4.3, the noise angular power spectrum is expected to drop from 10^{-19} to $\approx 6 \cdot 10^{-24}$ for the dipole $\ell = 1$.

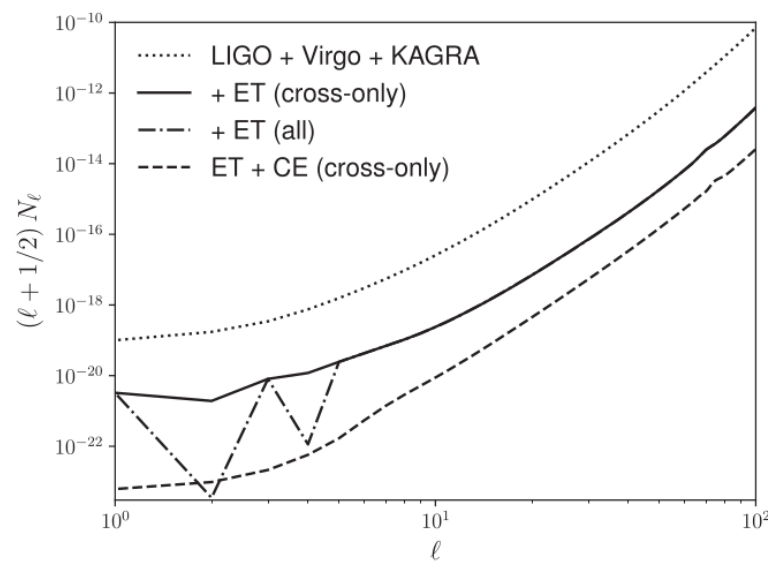


Figure 4.3: The noise angular power spectrum for different detectors at a reference frequency of 63 Hertz. LVK a the dotted line, ET in solid and dot-dashed lines and CE in a dashed line. This figure is taken from Alonso et al. 2020.

5

Information Field Theory

Since the noise in GW detectors is very high, especially compared to the GW background, it makes sense to use powerful methods to separate the signal from the noise. One promising method is information field theory (IFT). Information field theory is a technique for signal reconstruction and field inference designed by Torsten Enßlin and his group at the Max Planck Institute in Garching. Its goal is to use a formalism from Bayesian statistics and quantum field theory to be able to reuse methods to infer fields from data. The problem at the base is that we want to infer a spatially continuously distributed field from a finite amount of data. To do that, we can add our knowledge about physical laws, statistics, etc. of the problem, in the form of correlation functions.

We need to define our probability density functions over the space of all possibilities, which is why we will integrate using path integrals in this formalism.

If we assume a linear measurement, our data consists of the signal modified by a response function and added noise.

$$d = Rs + n \quad (5.1)$$

It is reasonable to assume a linear response from our detector, see e.g. **todo satyaprakash**. They derive an expression for the return time of the laser signal in the interferometer derived by time. This is proportional to the time derivative of the strain, here in plus polarisation.

$$\frac{dt_{return}}{dt} = 1 + \sin^2(\theta)L\dot{h}_+(t) \quad (5.2)$$

Here, θ is the angle between the beam direction and the detector plane.

$$(Rs)_i = \int dx R_{ix} s_x \quad (5.3)$$

The response corresponds to the point spread function of our instrument and other linear operations performed on the data.

With Gaussian noise, we get the following likelihood:

$$P(d|s) = \mathcal{N}(d - Rs, N). \quad (5.4)$$

5.1 Information Hamiltonian

Using Bayes theorem, we define what is called an information Hamiltonian.

$$P(s|d) = \frac{P(d|s)P(s)}{P(d)} \quad (5.5)$$

$$= \frac{e^{-\mathcal{H}(d,s)}}{Z_d} \quad (5.6)$$

Here, Z_d is the partition function, which is the evidence here.

$$Z_d = P(d) \quad (5.7)$$

$$\mathcal{H}(d, s) = -\ln(P(d|s)) - \ln(P(s)) \quad (5.8)$$

5.2 Wiener Filter

For a Gaussian prior and a Gaussian signal, we obtain the following Hamiltonian.

$$\mathcal{H}(d, s) = \frac{1}{2}(d - Rs)^\dagger N^{-1}(d - Rs) + \frac{1}{2}s^\dagger S^{-1}s \quad (5.9)$$

With quadratic completion, we can rewrite this in canonical form.

$$\mathcal{H}(d, s) = \frac{1}{2}(s - m)^\dagger D^{-1}(s - m) \quad (5.10)$$

When applying the covariance to the source, we get the mean according to the Wiener filter.

$$m = Dj \quad (5.11)$$

$$D = (S^{-1} + R^\dagger N^{-1}R)^{-1} \quad (5.12)$$

$$j = R^\dagger N^{-1}d \quad (5.13)$$

The covariance can also be written with the signal and the mean:

$$D = \langle (s - m)(s - m)^\dagger \rangle_{s|d} \quad (5.14)$$

Here, we assume the detector response R , the noise covariance N of the detector and the signal covariance S coming from physical laws, here coming from the calculated angular power spectrum.

The posterior of the Wiener filter is a Gaussian distribution with mean $s - m$ and the earlier-mentioned covariance.

$$P(s|d) = \mathcal{N}(s - m, D) \quad (5.15)$$

5.3 1D Toy Model

To show how NIFTy works in principle, we will reconstruct a one-dimensional power spectrum. From this input, a random realisation of data points is drawn from which the signal is reconstructed. The reconstruction and the residual plot are shown in Fig. 5.1. In this case, the reconstruction works quite well.

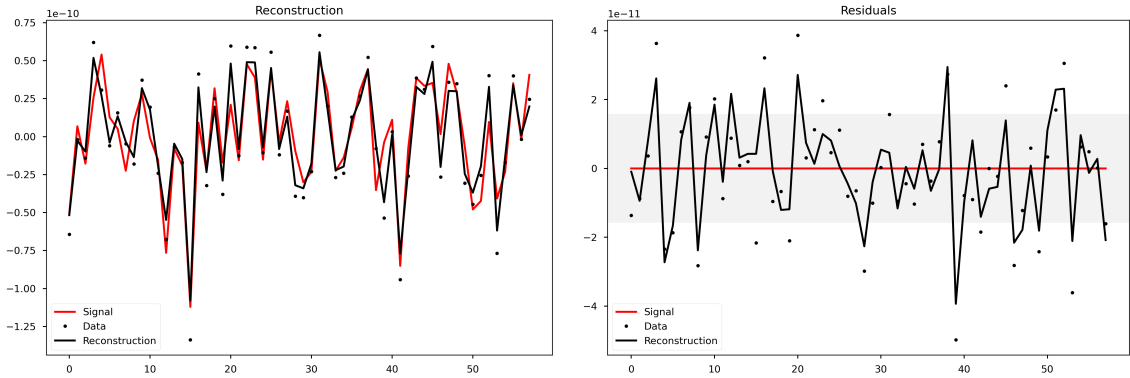


Figure 5.1: An example of using the NIFTy code to reconstruct an input power spectrum.

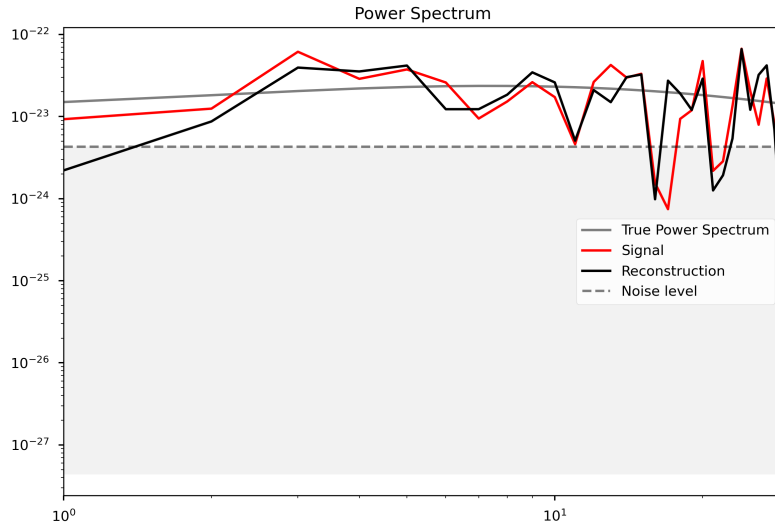


Figure 5.2: The power spectra of the one-dimensional toy model. The input power spectrum is shown in grey, the signal realisation in red and the reconstruction using IFT in black.

In Fig. 5.2, we show different power spectra, i.e. the input, the one from the randomly drawn signal and the reconstruction. The reconstruction power spectrum is very similar to the signal one in this toy model.

6

Results

To get a frequency-dependent angular power spectrum from `Multi_CLASS`, we implemented a frequency-dependent window function (see 3.5) and evolution bias (see 3.7). Using this, we can choose a measured GW frequency as an input parameter and compute the angular power spectrum. We extended the `Multi_CLASS` code to also include the dipole $l = 1$, since the standard code starts at the quadrupole $l = 2$.

6.1 Frequency Dependent AGWB Angular Power Spectrum

In Fig.6.1, the AGWB angular power spectra are plotted for different observed frequencies. The maximum multipole calculated here is $\ell = 30$ which is relatively high for GW detectors, see 4.3. The noise power spectrum increases similarly at all multipoles, so the cutoff is slightly arbitrary. Using our formalism in `Multi_CLASS`, it is easy to calculate the anisotropies up to arbitrary high multipoles, only taking linearly more computation time. The frequency range here goes from 10 to 10000 Hertz. However, as noted in section 2.2.1, the approximation to neglect neutron star mergers is not valid going much above 1000 Hertz.

There is a clear frequency dependence of the angular power spectra ranging around one and a half orders of magnitude. We can see that the highest angular power spectrum occurs at 400 Hertz while the lowest is at 100 Hertz. If we focus on the dipole $l = 1$, we can plot it as a function of frequency, see Fig.6.3b. The shape loosely resembles the energy spectrum in Fig. 3.2 which also peaks at around 400 Hertz and has a minimum at around 100 Hertz. the window function depends on frequency in through this energy spectrum multiplied by f and divided by the monopole.

$$\tilde{W}(z, f_o) \propto \frac{dE_{GW}/(df_e d\Omega_e) (f_e)}{\int dz (1+z)^{-1} H(z)^{-1} R_{BBH}(z) dE_{GW}/(df_e d\Omega_e) (f_e)} \quad (6.1)$$

To compare our results, we use Dall’Armi, Ricciardone, and Bertacca 2022 and their frequency-dependent dipole in Fig. 6.3. They additionally computed the kinematic dipole coming from our observer velocity with respect to the rest frame of the large scale structure. Furthermore, they considered the shot noise. This is the variance from a Poisson distribution which the GW mergers follow. We compare our intrinsic anisotropies with theirs in blue. The rough shape of our calculation looks

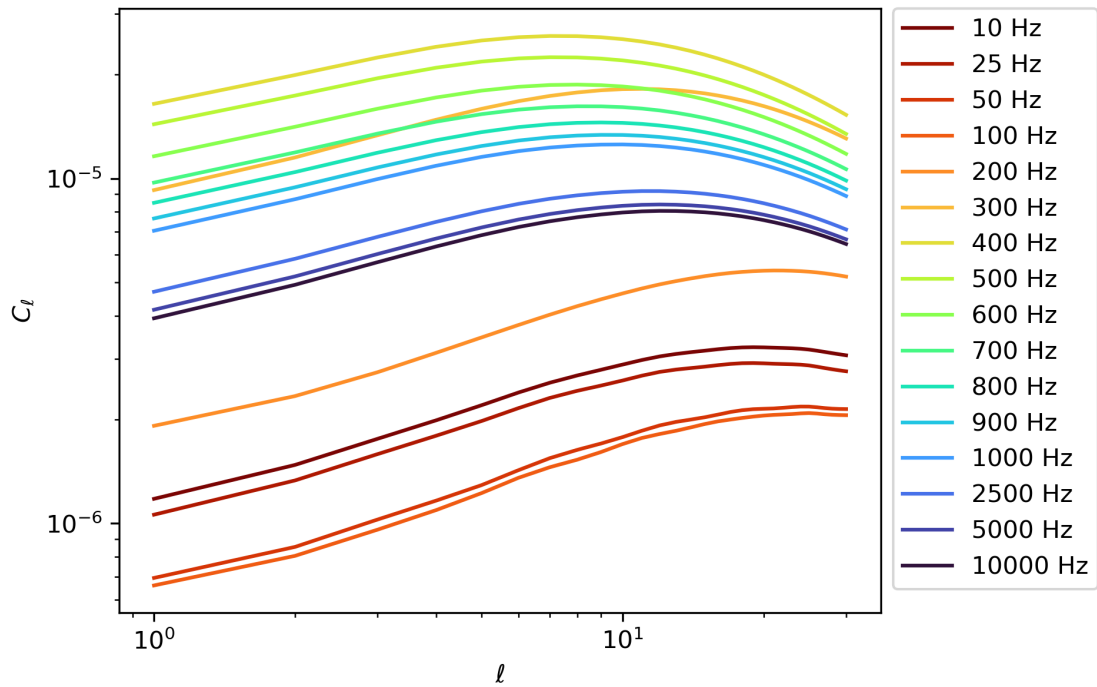


Figure 6.1: AGWB angular power spectrum of different observed frequencies, going up to $\ell = 30$.

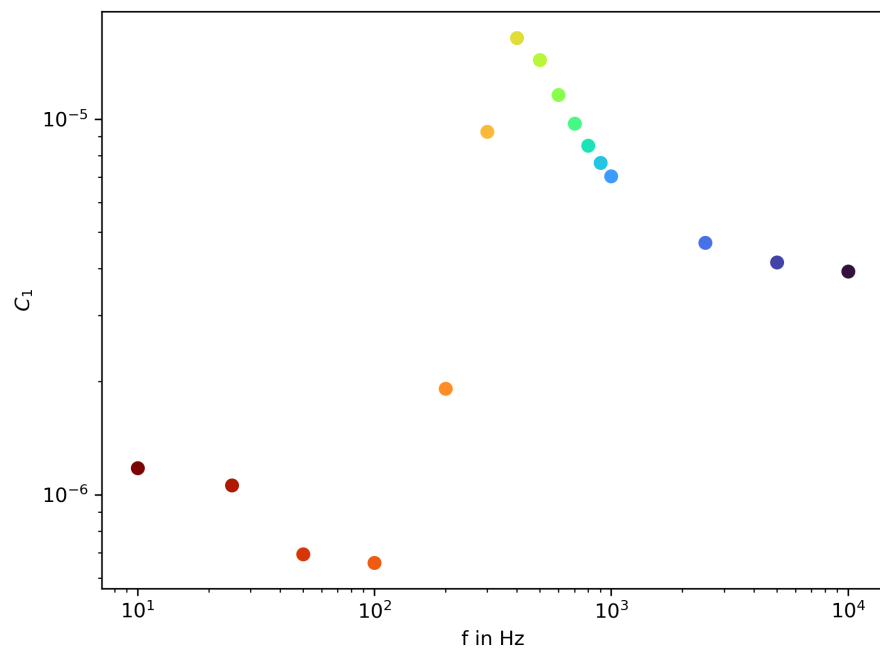


Figure 6.2: The dipole of the AGWB at different observed frequencies.

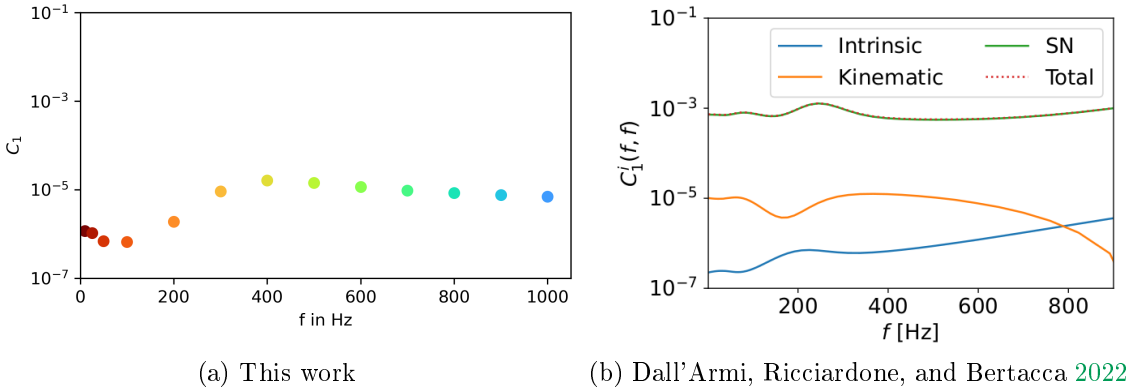


Figure 6.3: Comparison of the computed dipole contribution. On the left are the computed anisotropies using our formalism for the intrinsic anisotropies. On the right, the computed dipole by Dall’Armi, Ricciardone, and Bertacca 2022. The intrinsic dipole is shown in blue, the kinematic dipole in orange and the shot noise for the dipole in green.

similar, reaching a minimum at ≈ 100 Hertz, then peaking and declining again. In their plot, the peak is at ≈ 200 Hertz which is a lower frequency than ours. Additionally, they observe a continuous exponential increase (due to the lin-log axes) for frequencies above ≈ 400 Hertz. In this work this increase is not present. Even at higher frequencies up to 10,000 Hertz (see Fig. 6.3b) the dipole does not increase. Physically, higher frequencies correspond to a higher chirp mass M_c , so a binary with higher masses.

6.2 AGWB vs. Noise

To compare to the noise levels in section 4.2, we have to keep in mind that we calculated relative C_l with respect to the monopole. This is because we start with the density contrast in section 3.5.

$$\delta_{AGWB}(f_o, \hat{n}) = \frac{\Omega_{AGWB}(f_o, \hat{n}) - \bar{\Omega}_{AGWB}(f_o)}{\bar{\Omega}_{AGWB}(f_o)} \quad (6.2)$$

$$= \int dz \tilde{W}(f_o, z) \Delta_{AGWB}(f_o, \hat{n}, z) \quad (6.3)$$

Since the anisotropies are a two-point correlation, they depend quadratically on the source functions which come from the density contrast above.

$$C_l = 4\pi \int \frac{dk}{k} P(k) \Delta_l \Delta_l^* \quad (6.4)$$

Thus, to compute the physical angular power spectrum, we need to divide by the squared monopole over the solid angle.

$$C_l^{rel} = C_l \frac{(4\pi)^2}{\Omega_{GW}^2} \quad (6.5)$$

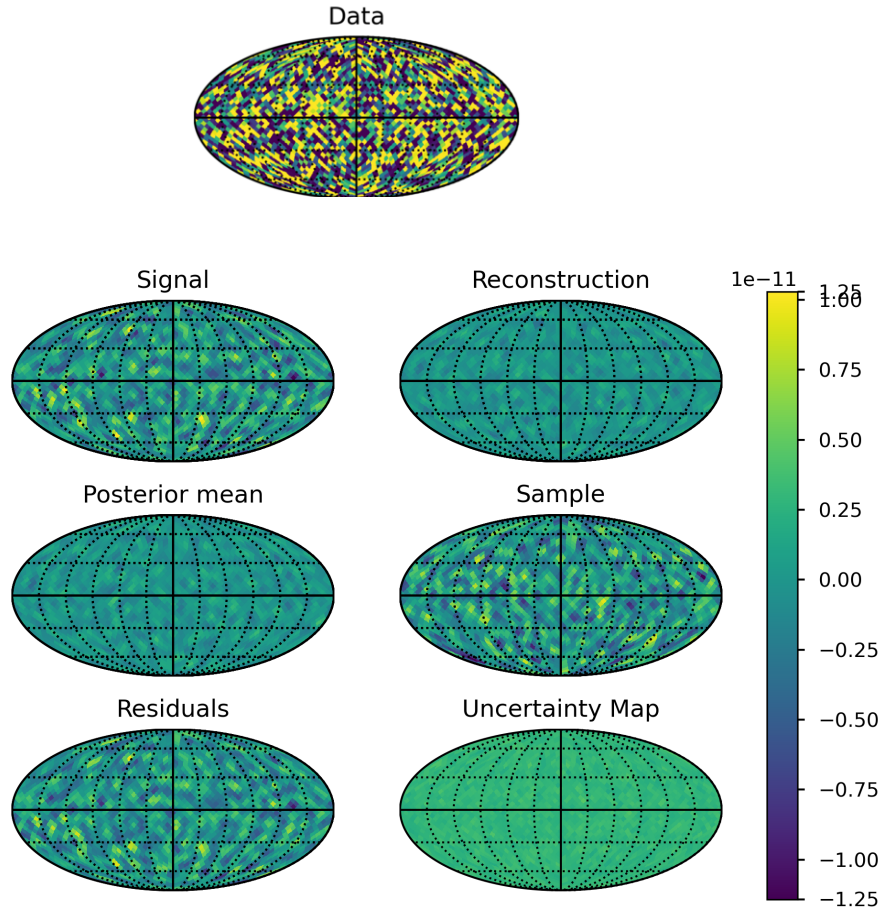


Figure 6.4: Reconstruction of the AGWB at 100 Hertz on a sky map using the NIFTy code. The data on top is generated from the signal which is a realisation of the input power spectrum. The posterior mean is calculated using a Wiener filter. A sample of this is drawn randomly. The residuals represent the difference between signal and reconstruction from the first row. The uncertainty map shows the calculated errors on the reconstruction.

For the noise angular power spectrum, we assume Gaussian noise using the best anisotropic noise sensitivity for ET and CE using cross-correlations (at $l = 1$). This is an optimistic assumption. The computed C_l used for the separation reach up to $l = 30$. Looking at Fig. 4.3, our assumed noise curve would have the shape of $l + \frac{1}{2}$ up to $l = 30$, which would increase more slowly than the actual sensitivity curve.

As seen in Fig. 6.1, we compute the lowest angular power spectrum at a frequency of 100 Hertz. To test the separation in this case, we use it as input for a reconstruction on a sky map using `HEALPix`; `healpix`. At this frequency, the separation is not

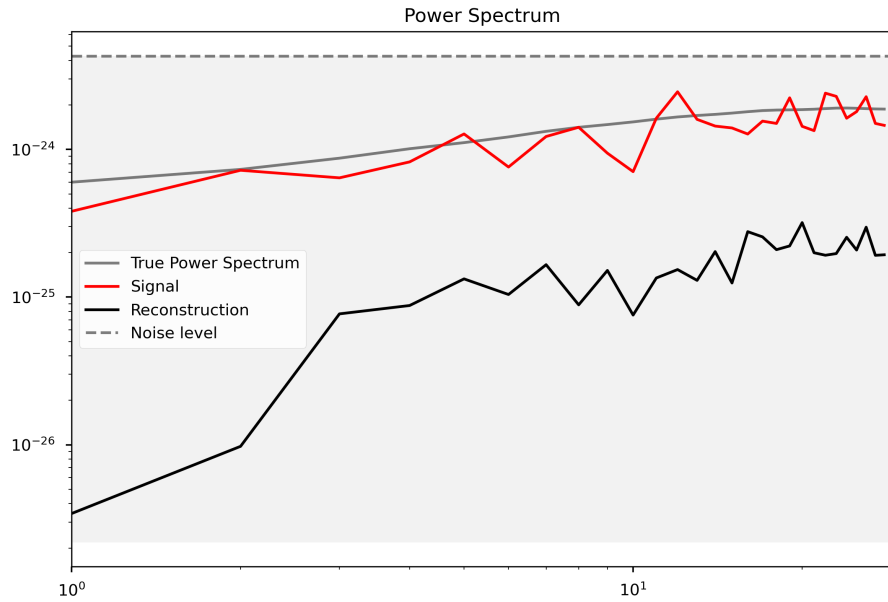


Figure 6.5: The power spectra of the AGWB separation at 100 Hertz. The input power spectrum is shown in grey, the signal realisation in red and the reconstruction using IFT in black.

successful. We see that the noise in the data in Fig. 6.4 is higher than the original signal. The posterior mean and the reconstruction are both close to zero. Thus, the sample also does not mimic the signal and the residuals have the same order of magnitude as the original signal.

In the power spectrum in Fig. 6.5, we can see that the noise is roughly one order of magnitude higher than the input power spectrum which explains why a separation is not possible. The reconstruction is much lower. By trying to filter out the noise, the signal gets filtered out as well in this case. To successfully separate the signal at 100 Hertz, we would need a detector that is around 2 orders of magnitude better in sensitivity compared to ET+CE.

The AGWB has the highest angular power spectrum at 400 Hertz in our calculation (see Fig. 6.1). So, we use this frequency to perform another IFT separation. In the separation in Fig. 6.6, the data resembles the signal more closely than for 100 Hertz. Comparing the signal to the reconstruction sky map, we see that most maxima and minima are recovered successfully. The posterior mean from the Wiener filter also mimics the signal map. When a sample is drawn from this posterior, it has some more pronounced minima and maxima but still follows the signal. However, our residuals have the same order of magnitude as the signal which is reflected in the uncertainty map as well.

In this case, the noise is half an order of magnitude lower than our power spectrum at 400 Hertz which is why the reconstruction is relatively successful, see Fig. 6.7. Regardless, the reconstruction is lower at all scales compared to the signal. If the detectors had a sensitivity of half or one order of magnitude lower, this reconstruction would be very feasible at 400 Hertz.

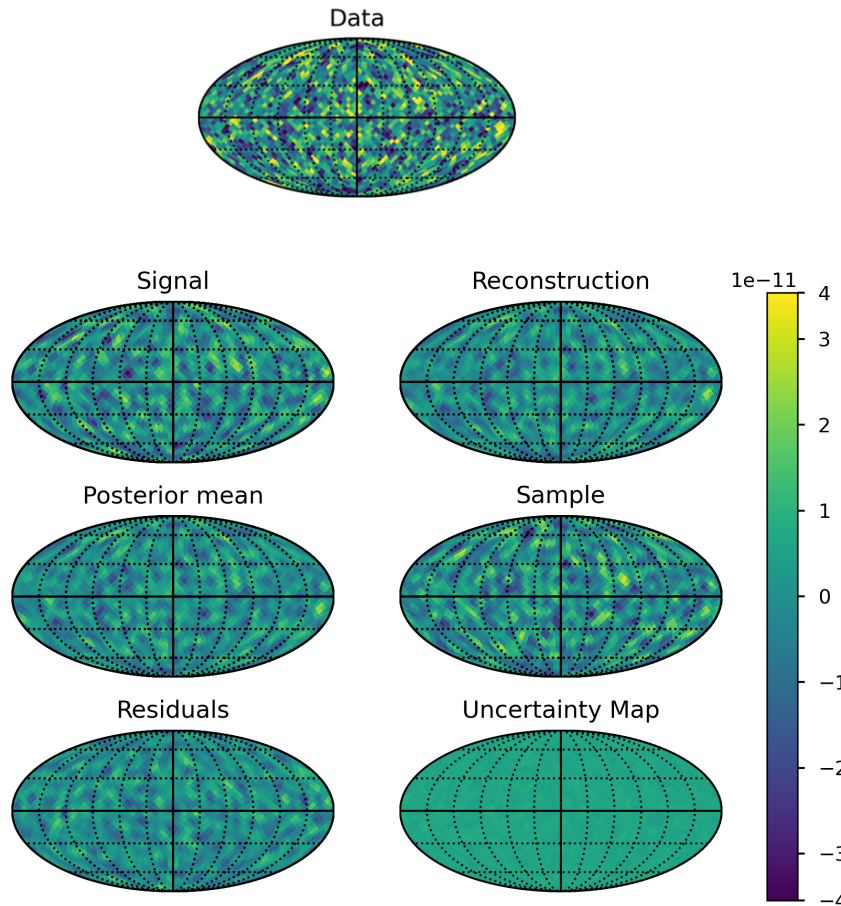


Figure 6.6: Reconstruction of the AGWB at 400 Hertz on a sky map using the `NIFTy` code. The data on top is generated from the signal which is a realisation of the input power spectrum. The posterior mean is calculated using a Wiener filter. A sample of this is drawn randomly. The residuals represent the difference between signal and reconstruction from the first row. The uncertainty map shows the calculated errors on the reconstruction.

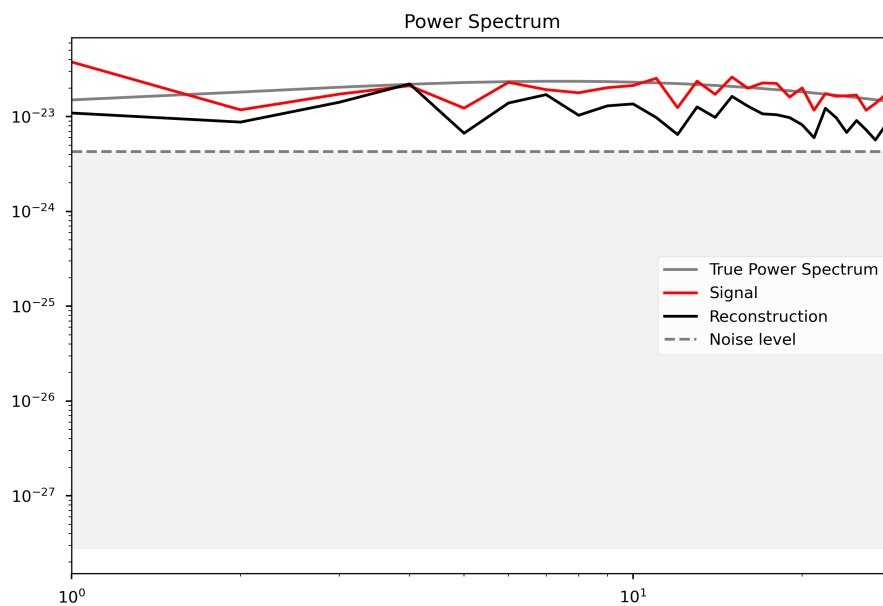


Figure 6.7: The power spectra of the AGWB separation at 400 Hertz. The input power spectrum is shown in grey, the signal realisation in red and the reconstruction using IFT in black.

6.3 CGWB vs. Noise

Ideally, we could also detect the cosmological GW background with future experiments. To see how feasible this is, we use the `GW_CLASS` code by Schulze et al. 2023 that is also based on `CLASS`.

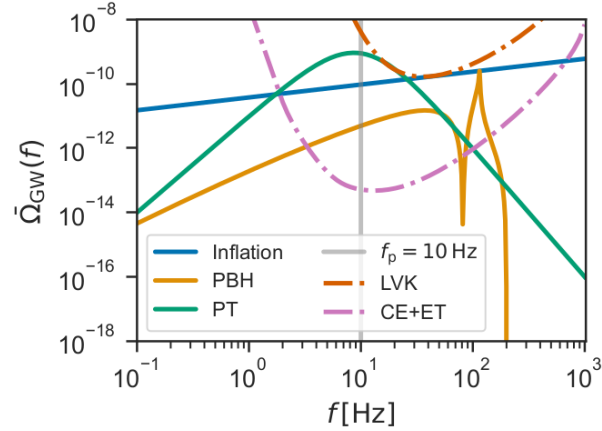


Figure 6.8: Frequency dependence of the monopole of the cosmological GW background for different generation mechanisms. The inflation scenario is shown in blue, primordial BH in orange and GW from phase transitions in green. The sensitivities for LVK and ET+CE are also shown for the monopole background.

We assume a cosmological GW background coming only from inflation, see section 2.2.2. This has a blue tilt, meaning the background increases with frequency. To see the frequency dependency, we can look at the monopole amplitude shown in Fig.6.8.

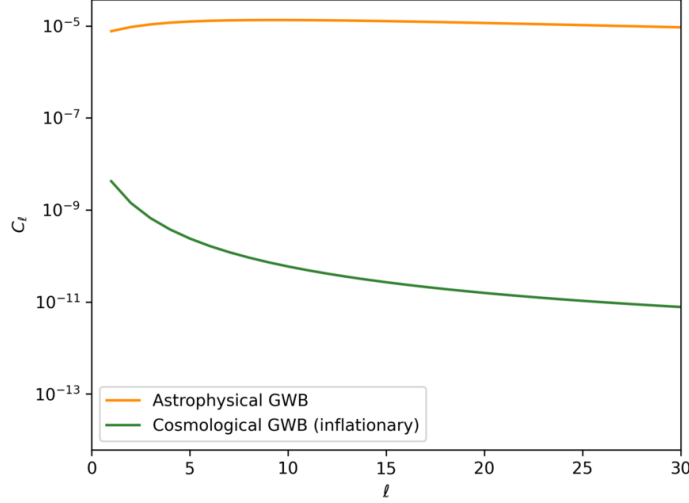


Figure 6.9: A comparison of the angular power spectra of the astrophysical versus the inflationary cosmological GW background at 900 Hertz.

Due to the blue tilt, we use a high frequency of 900 Hertz to test the IFT separation. The assumed noise is the same as for the AGWB case. Again, the relative C_ℓ

are converted into physical C_ℓ .

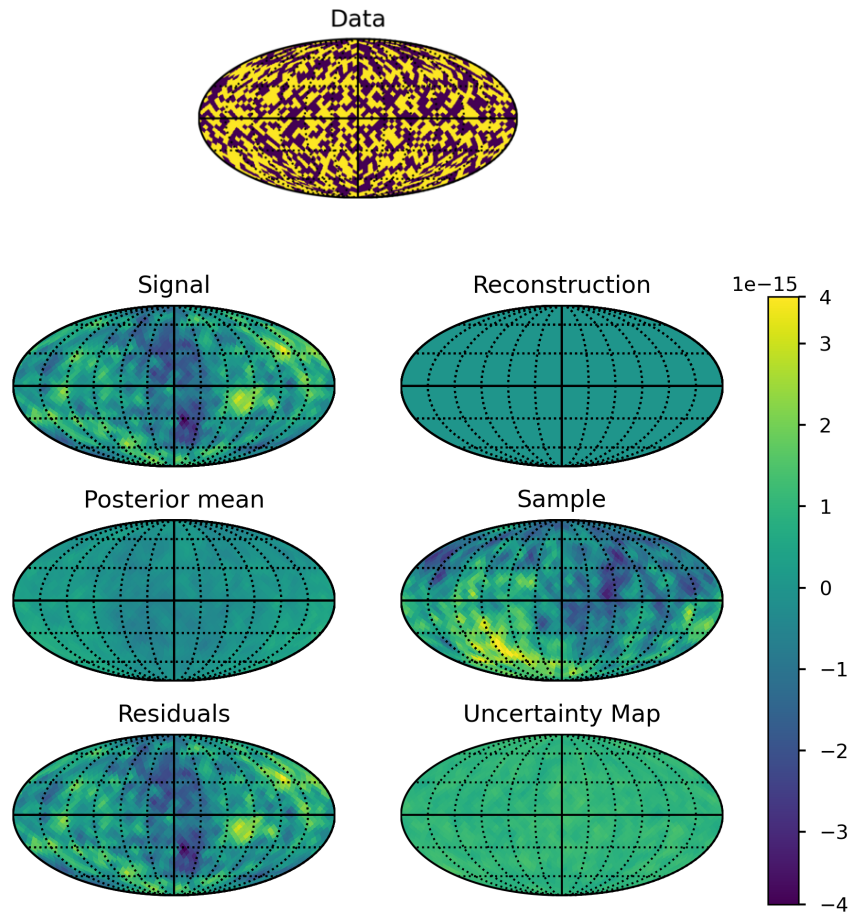


Figure 6.10: Reconstruction of the CGWB at 900 Hertz on a sky map using the `NIFTy` code. The data on top is generated from the signal which is a realisation of the input power spectrum. The posterior mean is calculated using a Wiener filter. A sample of this is drawn randomly. The residuals represent the difference between signal and reconstruction from the first row. The uncertainty map shows the calculated errors on the reconstruction.

In Fig. 6.10 it is visible that the data is much noisier than the signal computed from the cosmological power spectrum. The reconstruction is not possible, thus the reconstructed sky map and the posterior mean are near zero. The sample drawn from the posterior mean does not resemble the signal and the uncertainty map averages much higher than the reconstruction.

Looking at the power spectrum in Fig. 6.11, we see that the noise level is roughly five orders of magnitude higher than the input and signal. Like for the AGWB at 100 Hertz, the reconstruction is much lower than the signal, because it is filtered out together with the noise.

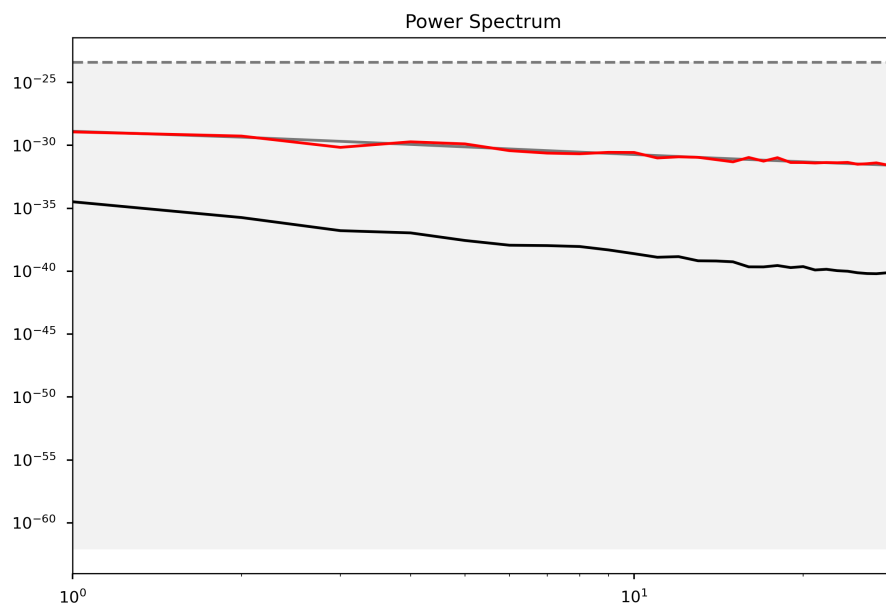


Figure 6.11: The power spectra of the CGWB separation at 900 Hertz. The input power spectrum is shown in grey, the signal realisation in red and the reconstruction using IFT in black.

7

Conclusion & Outlook

We considered the stochastic GW background of BBH using the number density distribution. We compute the angular power spectra of the AGWB using `Multi_CLASS` with a dependence on the measured frequency. We then use this result for an IFT separation with the `NIFTy` package.

For the noise power spectrum, we optimistically assume Gaussian noise. This could be made more realistic by using the ET spectrum directly for the separation.

In the future, it would be natural to extend this and use the frequency dependence directly in `NIFTy`. This should improve the separation since it is an extra dimension that can be used to perform the separation.

Appendix A

Call Graph? (TODO)

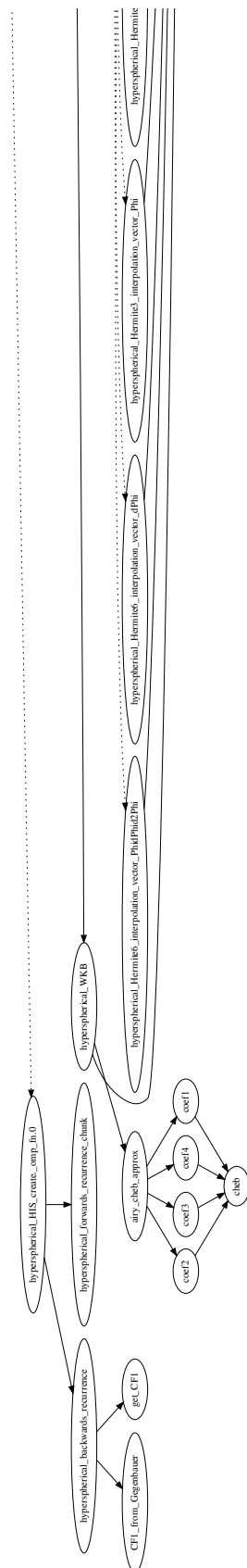


Figure A.1

List of Figures

2.1	Illustration of the plus and cross polarisations varying with time.	9
2.2	The GW energy density parameter as a function of frequency from 1 to 10,000 Hz.	13
2.3	The different stages of a BBH merger with the corresponding waveform.	14
3.1	The three phases of a binary coalescence: inspiral, merger and ringdown.	20
3.2	The energy spectrum as a function of frequency for a BBH merger where both BH have a mass of $20M_{\odot}$	21
3.3	The energy spectrum $d^2E_{GW,e}/df_e d\Omega_e$ at different observed frequencies as a function of redshift.	22
3.4	The SFR for star-forming galaxies for different redshifts.	24
3.5	The dimensionless HMF for different redshifts z at $\Delta = 800$	26
3.6	The HMF at $z = 0$	27
3.7	The BBH merger rate as a function of the redshift z	28
3.8	GW angular power spectrum for different window functions.	29
3.9	GW angular power spectrum for different redshifts.	29
3.10	The final window function at 1 Hertz for this code for comparison with Dall’Armi, Ricciardone, and Bertacca 2022.	30
3.11	The window functions at different observed frequencies.	31
3.12	The influence of the evolution bias on the angular power spectrum at an observed frequency of 1000 Hertz.	33
4.1	Design sensitivity curves for the LVK detector network.	34
4.2	The design sensitivity curve for ET and CE compared to LIGO A+.	35
4.3	The noise angular power spectrum for different detectors at a reference frequency of 63 Hertz.	36
5.1	An example of using the NIFTy code to reconstruct an input power spectrum.	39
5.2	The power spectra of the one-dimensional toy model.	39
6.1	AGWB angular power spectrum of different observed frequencies, going up to $l = 30$	41
6.2	The dipole of the AGWB at different observed frequencies.	41
6.3	Comparison of the computed dipole contribution to Dall’Armi, Ricciardone, and Bertacca 2022.	42
6.4	Reconstruction of the AGWB at 100 Hertz on a sky map using the NIFTy code.	43
6.5	The power spectra of the AGWB separation at 100 Hertz.	44

6.6	Reconstruction of the AGWB at 400 Hertz on a sky map using the NIFTy code.	45
6.7	The power spectra of the AGWB separation at 400 Hertz.	46
6.8	Frequency dependence of the monopole of the cosmological GW background for different generation mechanisms.	47
6.9	A comparison of the angular power spectra of the astrophysical versus the inflationary cosmological GW background at 900 Hertz.	47
6.10	Reconstruction of the CGWB at 900 Hertz on a sky map using the NIFTy code.	49
6.11	The power spectra of the CGWB separation at 900 Hertz.	50
A.1	53

List of Tables

3.1	Amplitude parameters with and without the zero spin approximation.	20
-----	--	----

Acknowledgements

I would like to thank my supervisors Prof. Dr. Philipp Mertsch and Prof. Dr. Julien Lesgourgues. Lorenzo Valbusa Dall’Armi also offered his expertise on gravitational waves and kindly provided some of his data to compare with my code. Additionally, Sefa Pamuk, Tobias Thrien and Christian Radermacher were always happy to discuss physical concepts and provide help regarding the CLASS code. Laurin Söding helped me with some concerns regarding the NIFTy code, as well. Lastly, thanks to Clemens Panitz and Sefa Pamuk? for proofreading this thesis.

Bibliography

- Agazie, Gabriella et al. (June 28, 2023). *The NANOGrav 15-year Data Set: Evidence for a Gravitational-Wave Background*. DOI: [10.3847/2041-8213/acdac6](https://doi.org/10.3847/2041-8213/acdac6). arXiv: [2306.16213\[astro-ph, physics:gr-qc\]](https://arxiv.org/abs/2306.16213). URL: <http://arxiv.org/abs/2306.16213> (visited on 09/15/2023).
- Holten, J. W. van (Mar. 2019). “Gravitational waves from generalized newtonian sources”. In: *Fortschritte der Physik* 67.3, p. 1800083. ISSN: 00158208. DOI: [10.1002/prop.201800083](https://doi.org/10.1002/prop.201800083). arXiv: [1809.05670\[astro-ph, physics:gr-qc\]](https://arxiv.org/abs/1809.05670). URL: <http://arxiv.org/abs/1809.05670> (visited on 09/11/2023).
- Collaboration, The LIGO Scientific et al. (Feb. 23, 2022). *The population of merging compact binaries inferred using gravitational waves through GWTC-3*. arXiv: [2111.03634\[astro-ph, physics:gr-qc\]](https://arxiv.org/abs/2111.03634). URL: <http://arxiv.org/abs/2111.03634> (visited on 10/04/2023).
- Capurri, Giulia et al. (Nov. 1, 2021). “Intensity and anisotropies of the stochastic Gravitational Wave background from merging compact binaries in galaxies”. In: *Journal of Cosmology and Astroparticle Physics* 2021.11, p. 032. ISSN: 1475-7516. DOI: [10.1088/1475-7516/2021/11/032](https://doi.org/10.1088/1475-7516/2021/11/032). arXiv: [2103.12037\[astro-ph, physics:gr-qc\]](https://arxiv.org/abs/2103.12037). URL: <http://arxiv.org/abs/2103.12037> (visited on 09/22/2023).
- Abbott, B. P. et al. (Feb. 11, 2016). “Observation of Gravitational Waves from a Binary Black Hole Merger”. In: *Physical Review Letters* 116.6, p. 061102. ISSN: 0031-9007, 1079-7114. DOI: [10.1103/PhysRevLett.116.061102](https://doi.org/10.1103/PhysRevLett.116.061102). URL: <https://link.aps.org/doi/10.1103/PhysRevLett.116.061102> (visited on 09/01/2023).
- Christensen, Nelson (Jan. 1, 2019). “Stochastic gravitational wave backgrounds”. In: *Reports on Progress in Physics* 82.1, p. 016903. ISSN: 0034-4885, 1361-6633. DOI: [10.1088/1361-6633/aae6b5](https://doi.org/10.1088/1361-6633/aae6b5). URL: <https://iopscience.iop.org/article/10.1088/1361-6633/aae6b5> (visited on 08/10/2023).
- Phinney, E. S. (Aug. 1, 2001). *A Practical Theorem on Gravitational Wave Backgrounds*. arXiv: [astro-ph/0108028](https://arxiv.org/abs/astro-ph/0108028). URL: <http://arxiv.org/abs/astro-ph/0108028> (visited on 09/15/2023).
- Schulze, Florian et al. (May 2, 2023). *GW_CLASS: Cosmological Gravitational Wave Background in the Cosmic Linear Anisotropy Solving System*. arXiv: [2305.01602\[astro-ph, physics:gr-qc\]](https://arxiv.org/abs/2305.01602). URL: <http://arxiv.org/abs/2305.01602> (visited on 08/10/2023).
- Blas, Diego, Julien Lesgourgues, and Thomas Tram (July 1, 2011). “The Cosmic Linear Anisotropy Solving System (CLASS) II: Approximation schemes”. In: *Journal of Cosmology and Astroparticle Physics* 2011.7, pp. 034–034. ISSN: 1475-7516.

- DOI: [10.1088/1475-7516/2011/07/034](https://doi.org/10.1088/1475-7516/2011/07/034). arXiv: [1104.2933\[astro-ph\]](https://arxiv.org/abs/1104.2933). URL: <http://arxiv.org/abs/1104.2933> (visited on 09/15/2023).
- Alonso, David et al. (June 22, 2020). “Noise angular power spectrum of gravitational wave background experiments”. In: *Physical Review D* 101.12, p. 124048. ISSN: 2470-0010, 2470-0029. DOI: [10.1103/PhysRevD.101.124048](https://doi.org/10.1103/PhysRevD.101.124048). URL: <https://link.aps.org/doi/10.1103/PhysRevD.101.124048> (visited on 08/10/2023).
- Robson, Travis, Neil Cornish, and Chang Liu (May 23, 2019). “The construction and use of LISA sensitivity curves”. In: *Classical and Quantum Gravity* 36.10, p. 105011. ISSN: 0264-9381, 1361-6382. DOI: [10.1088/1361-6382/ab1101](https://doi.org/10.1088/1361-6382/ab1101). arXiv: [1803.01944\[astro-ph, physics:gr-qc\]](https://arxiv.org/abs/1803.01944). URL: <http://arxiv.org/abs/1803.01944> (visited on 09/22/2023).
- Scelfo, Giulio et al. (Sept. 25, 2018). “GW\$\\times\$LSS: Chasing the Progenitors of Merging Binary Black Holes”. In: *Journal of Cosmology and Astroparticle Physics* 2018.9, pp. 039–039. ISSN: 1475-7516. DOI: [10.1088/1475-7516/2018/09/039](https://doi.org/10.1088/1475-7516/2018/09/039). arXiv: [1809.03528\[astro-ph, physics:gr-qc\]](https://arxiv.org/abs/1809.03528). URL: <http://arxiv.org/abs/1809.03528> (visited on 08/10/2023).
- Di Dio, Enea et al. (Nov. 20, 2013). “The CLASSgal code for Relativistic Cosmological Large Scale Structure”. In: *Journal of Cosmology and Astroparticle Physics* 2013.11, pp. 044–044. ISSN: 1475-7516. DOI: [10.1088/1475-7516/2013/11/044](https://doi.org/10.1088/1475-7516/2013/11/044). arXiv: [1307.1459\[astro-ph\]](https://arxiv.org/abs/1307.1459). URL: <http://arxiv.org/abs/1307.1459> (visited on 08/09/2023).
- Dall’Armi, Lorenzo Valbusa, Angelo Ricciardone, and Daniele Bertacca (Nov. 1, 2022). “The Dipole of the Astrophysical Gravitational-Wave Background”. In: *Journal of Cosmology and Astroparticle Physics* 2022.11, p. 040. ISSN: 1475-7516. DOI: [10.1088/1475-7516/2022/11/040](https://doi.org/10.1088/1475-7516/2022/11/040). arXiv: [2206.02747\[astro-ph, physics:gr-qc\]](https://arxiv.org/abs/2206.02747). URL: <http://arxiv.org/abs/2206.02747> (visited on 02/06/2023).
- Kaiser, Nick (July 1987). “Clustering in real space and in redshift space”. In: *Monthly Notices of the Royal Astronomical Society* 227.1, pp. 1–21. ISSN: 0035-8711, 1365-2966. DOI: [10.1093/mnras/227.1.1](https://doi.org/10.1093/mnras/227.1.1). URL: <https://academic.oup.com/mnras/article-lookup/doi/10.1093/mnras/227.1.1> (visited on 10/02/2023).
- Bellomo, Nicola et al. (Oct. 6, 2020). “Beware of commonly used approximations I: errors in forecasts”. In: *Journal of Cosmology and Astroparticle Physics* 2020.10, pp. 016–016. ISSN: 1475-7516. DOI: [10.1088/1475-7516/2020/10/016](https://doi.org/10.1088/1475-7516/2020/10/016). arXiv: [2005.10384\[astro-ph\]](https://arxiv.org/abs/2005.10384). URL: <http://arxiv.org/abs/2005.10384> (visited on 08/10/2023).
- Ajith, P. et al. (June 15, 2011). “Inspiral-merger-ringdown waveforms for black-hole binaries with non-precessing spins”. In: *Physical Review Letters* 106.24, p. 241101. ISSN: 0031-9007, 1079-7114. DOI: [10.1103/PhysRevLett.106.241101](https://doi.org/10.1103/PhysRevLett.106.241101). arXiv: [0909.2867\[astro-ph, physics:gr-qc\]](https://arxiv.org/abs/0909.2867). URL: <http://arxiv.org/abs/0909.2867> (visited on 02/06/2023).
- Bardeen, James M., William H. Press, and Saul A. Teukolsky (Dec. 1972). “Rotating Black Holes: Locally Nonrotating Frames, Energy Extraction, and Scalar Synchrotron Radiation”. In: *The Astrophysical Journal* 178, p. 347. ISSN: 0004-637X, 1538-4357. DOI: [10.1086/151796](https://doi.org/10.1086/151796). URL: <http://adsabs.harvard.edu/doi/10.1086/151796> (visited on 10/03/2023).

- Maggiore, Michele (2008). *Gravitational waves*. OCLC: 262833538. Oxford: Oxford University Press. ISBN: 978-0-19-171766-6.
- Behroozi, Peter et al. (Sept. 21, 2019). “UniverseMachine: The Correlation between Galaxy Growth and Dark Matter Halo Assembly from $z=0-10$ ”. In: *Monthly Notices of the Royal Astronomical Society* 488.3, pp. 3143–3194. ISSN: 0035-8711, 1365-2966. DOI: [10.1093/mnras/stz1182](https://doi.org/10.1093/mnras/stz1182). arXiv: [1806.07893 \[astro-ph\]](https://arxiv.org/abs/1806.07893). URL: <http://arxiv.org/abs/1806.07893> (visited on 02/06/2023).
- Klypin, Anatoly A., Sebastian Trujillo-Gomez, and Joel Primack (Oct. 20, 2011). “DARK MATTER HALOS IN THE STANDARD COSMOLOGICAL MODEL: RESULTS FROM THE BOLSHOI SIMULATION”. In: *The Astrophysical Journal* 740.2, p. 102. ISSN: 0004-637X, 1538-4357. DOI: [10.1088/0004-637X/740/2/102](https://doi.org/10.1088/0004-637X/740/2/102). URL: <https://iopscience.iop.org/article/10.1088/0004-637X/740/2/102> (visited on 10/02/2023).
- Klypin, Anatoly et al. (Apr. 21, 2016). “MultiDark simulations: the story of dark matter halo concentrations and density profiles”. In: *Monthly Notices of the Royal Astronomical Society* 457.4, pp. 4340–4359. ISSN: 0035-8711, 1365-2966. DOI: [10.1093/mnras/stw248](https://doi.org/10.1093/mnras/stw248). URL: <https://academic.oup.com/mnras/article-lookup/doi/10.1093/mnras/stw248> (visited on 10/02/2023).
- Abazajian, Kevork N. et al. (June 1, 2009). “THE SEVENTH DATA RELEASE OF THE SLOAN DIGITAL SKY SURVEY”. In: *The Astrophysical Journal Supplement Series* 182.2, pp. 543–558. ISSN: 0067-0049, 1538-4365. DOI: [10.1088/0067-0049/182/2/543](https://doi.org/10.1088/0067-0049/182/2/543). URL: <https://iopscience.iop.org/article/10.1088/0067-0049/182/2/543> (visited on 10/02/2023).
- McCracken, H. J. et al. (Aug. 2012). “UltraVISTA: a new ultra-deep near-infrared survey in COSMOS”. In: *Astronomy & Astrophysics* 544, A156. ISSN: 0004-6361, 1432-0746. DOI: [10.1051/0004-6361/201219507](https://doi.org/10.1051/0004-6361/201219507). URL: <http://www.aanda.org/10.1051/0004-6361/201219507> (visited on 10/02/2023).
- Bertacca, Daniele et al. (May 11, 2020). “Projection effects on the observed angular spectrum of the astrophysical stochastic gravitational wave background”. In: *Physical Review D* 101.10, p. 103513. ISSN: 2470-0010, 2470-0029. DOI: [10.1103/PhysRevD.101.103513](https://doi.org/10.1103/PhysRevD.101.103513). arXiv: [1909.11627 \[astro-ph, physics:gr-qc\]](https://arxiv.org/abs/1909.11627). URL: <http://arxiv.org/abs/1909.11627> (visited on 08/10/2023).